

Self-gravitating equilibrium models of dwarf galaxies and the minimum mass for star formation

Eduard I. Vorobyov,^{1,2} Simone Recchi,¹ and Gerhard Hensler,¹

¹ University of Vienna, Institute of Astrophysics, Vienna, 1180, Austria

² Research Institute of Physics, Southern Federal University, Rostov-on-Don, 344090 Russia

Accepted by A&A on May 4, 2012

ABSTRACT

We construct a series of model galaxies in rotational equilibrium consisting of gas, stars, and a fixed dark matter (DM) halo and study how these equilibrium systems depend on the mass and form of the DM halo, gas temperature, non-thermal and rotation support against gravity, and also on the redshift of galaxy formation. For every model galaxy we find the minimum gas mass $M_{\text{g}}^{\text{min}}$ required to achieve a state in which star formation (SF) is allowed according to contemporary SF criteria. The obtained $M_{\text{g}}^{\text{min}}-M_{\text{DM}}$ relations are compared against the baryon-to-DM mass relation $M_{\text{b}}-M_{\text{DM}}$ inferred from the Λ CDM theory and WMAP4 data. Our aim is to construct realistic initial models of dwarf galaxies (DGs), which take into account the gas self-gravity and can be used as a basis to study the dynamical and chemical evolution of DGs. Rotating equilibria are found by solving numerically the steady-state momentum equation for the gas component in the combined gravitational potential of gas, stars, and DM halo using a forward substitution procedure. We find that for a given M_{DM} the value of $M_{\text{g}}^{\text{min}}$ depends crucially on the gas temperature T_{g} , gas spin parameter α , degree of non-thermal support σ_{eff} , and somewhat on the redshift for galaxy formation z_{gf} . Depending on the actual values of T_{g} , α , σ_{eff} , and z_{gf} , model galaxies may have $M_{\text{g}}^{\text{min}}$ that are either greater or smaller than M_{b} . Galaxies with $M_{\text{DM}} \gtrsim 10^9 M_{\odot}$ are usually characterized by $M_{\text{g}}^{\text{min}} \lesssim M_{\text{b}}$, implying that SF in such objects is a natural outcome as the required gas mass is consistent with what is available according to the Λ CDM theory. On the other hand, models with $M_{\text{DM}} \lesssim 10^9 M_{\odot}$ are often characterized by $M_{\text{g}}^{\text{min}} \gg M_{\text{b}}$, implying that they need much more gas than available to achieve a state in which SF is allowed. Our modeling suggests that a star-formation-allowed state is more difficult to achieve in DM halos with mass $\lesssim 10^9 M_{\odot}$ than in their upper-mass counterparts, because the required gas mass often exceeds both M_{b} and M_{DM} . In the framework of the Λ CDM theory, this implies the existence of a critical DM halo mass below which the likelihood of star formation and hence the total stellar mass may drop substantially, in accordance with the stellar versus DM halo mass relations recently derived from the SDSS survey and Millennium Simulations. On the other hand, DGs that do not follow the Λ CDM trend are feasible and have recently been identified, which raises questions about the universality of the Λ CDM paradigm.

Key words. Galaxies: dwarf – galaxies: structure – ISM: structure – Stars: formation – dark matter – Methods: numerical

1. Introduction

The study of equilibrium states of self-gravitating, multi-component fluids is of considerable interest in astronomy because they serve as basic models of many astrophysical objects (stars, protoplanetary disks, galaxies among others). While it is known (and quite obvious from simple symmetry considerations) that isolated, non-rotating, self-gravitating fluids of finite extent must be spherically symmetric, it has been a formidable endeavour for some of the most distinguished astronomers and mathematicians of the last three centuries to discover the figures of equilibrium in the presence of rotation. In particular, the discovery of Jacobi in 1834 that equilibrium figures of uniformly rotating fluids need not be axisymmetric took the scientific community by surprise. The formidable body of knowledge on (incompressible and uniformly rotating) equilibrium figures has been filled up, corrected and consolidated only recently (Chandrasekhar, 1969; Tassoul, 1978).

Unfortunately, this knowledge has proven to be inadequate for the study of equilibrium configurations in galaxies mainly for two reasons: (i) the gas in galaxies is not incompressible, (ii) galaxies are not uniformly rotating. Fortunately enough, non-axisymmetric structures of equilibrium are secularly transformed into axisymmetric figures in realistic (compressible,

viscous and differentially rotating) models of galaxies (e.g. Lindblom, 1992). It is therefore always realistic to assume that the equilibrium configuration of a galaxy rotating about some axis is axisymmetric. It is however not always true that this figure of equilibrium is an ellipsoid. Rapidly rotating, compressible gases characterized by a polytropic equation of state quite naturally develop a flared structure (Bodenheimer & Ostriker, 1973; Tassoul, 1978). Flaring gas distributions in some DGs have been inferred (O'Brien et al., 2010; Banerjee et al., 2011) but direct observations of flaring gas disks are technically very difficult, even if DGs are edge-on (Sancisi & Allen, 1979). Nevertheless, moderate flaring have been observed in the Galaxy (Kent et al., 1991; Kalberla & Kerp, 2009) and in M31 (Brinks & Burton, 1984) and it is thus reasonable to expect flaring also in some gas-rich DGs. Because of the complex geometries (and, often, of the rotation curves) of realistic galaxies, it is extremely complex (if not impossible) to analytically compute figures of equilibrium and one must resort to numerical methods.

An equilibrium model without gas self-gravity suffers from two major drawbacks. First, such models cannot in principle be used to infer equilibrium configurations prone to star formation since the star formation criteria explicitly or implicitly rely on self-gravity as one of the key ingredients for star formation. This lack of self-consistency may lead to situa-

tions when the star formation feedback due to supernova explosions is studied in models that are insusceptible to star formation in the first place. Second, neglecting gas self-gravity one runs the risk of building a gravitationally overstable configuration, which would have never been realized if self-gravity were taken into account. Such a non-self-gravitating configuration would have too much gas compared to the self-gravitating counterpart and additional theoretical or empirical criteria are usually invoked to constrain the total gas mass (see e.g. Mac Low & Ferrara, 1999; Vasiliev et al., 2008). Moreover, the energy release and the corresponding SF rates are often set arbitrarily (e.g. Mac Low & Ferrara, 1999).

This paper is the first of a series of works dealing with the dynamical and chemical evolution of gas and stars in DGs embedded in dark matter (DM) halos. In the context, achieving an initial equilibrium configuration is clearly necessary in order to study how the onset of an episode of star formation or of another perturbing phenomenon affects the evolution of the studied object. Surprisingly, almost all the papers on this subject neglect self-gravity of gas and stars and consider a simplified initial equilibrium configuration, namely a rotating isothermal gas distribution in hydrostatic equilibrium with a fixed potential well (a DM halo or a static distribution of stars; see e.g. Suchkov et al., 1994; Mac Low & Ferrara, 1999; Strickland & Stevens, 2000; Recchi et al., 2001; Marcolini et al., 2003; Vorobyov et al., 2004; Scannapieco & Brügggen, 2010, among many others).

In this work, we solve numerically the steady-state momentum equation of a multi-component galaxy (made of gas, stars and a DM halo) taking into account the gravitational acceleration of all these components. This task has been attempted only by very few authors (Narayan & Jog, 2002; Harfst et al., 2006; Banerjee et al., 2011). The typical justification for neglecting gas self-gravity in constructing initial equilibrium models for DGs is that “the gravitational potential of DGs with $M_g \lesssim 10^9 M_\odot$ is dominated by the dark matter halo” (Mac Low & Ferrara, 1999). However, it is worth reminding that some authors still doubt about the presence of massive DM halos around DGs. For instance, recent observations of the mass-to-light ratios in Virgo Cluster dwarf ellipticals by Toloba et al. (2011) and in gas-rich DGs by Swaters et al. (2011) and also studies of structural properties of the Milky Way dwarf spheroidals (see e.g. Kroupa et al., 2010, and references therein) are substantially questioning the contribution of DM on small scales.

Moreover (and more importantly), even if the total mass of a dwarf galaxy is dominated by a DM halo, within the Holmberg radius most of the galaxy is made of baryons (see e.g. Papaderos et al., 1996; Swaters et al., 2011), although some authors report different claims (e.g. Carignan & Beaulieu, 1989). In some numerical works (which neglect gas self-gravity) it can be clearly noticed that the assumed DM profile leads to a very low density of the DM component (much lower than the gas density) in the central region of the simulated galaxy (for instance in D’Ercole & Brighenti, 1999, the central gas density is ~ 10 times larger than the DM density). Central densities of the DM halos in DGs can also be inferred from the observed rotation curves and typical values are quite low; significantly below $10^{-24} \text{ g cm}^{-3}$ (de Blok et al., 2008). We can thus conclude that it is very unlikely that gas self-gravity is negligible in the central parts of gas-rich DGs. All the above arguments in favour of gas self-gravity justify the relevance of the present study.

The plan of the paper is as follows. The basics of the numerical model are described in Section 2. The initial and boundary conditions, as well as the solution procedure, are summarized in Section 3. The main results are presented in Sections 4 and

5. A comparison of our results with predictions of the Λ CDM theory is given in Section 6. The implications for the evolution of DGs and the model caveats are discussed in Sections 7 and 8, respectively. The main conclusions are summarized in Section 9.

2. Numerical model

An accurate construction of self-gravitating, rotating equilibria involves solving for the steady-state momentum equations of gas, stars, and dark matter in their combined gravitational potential. This is however a difficult and time consuming numerical exercise, since the density distribution of each component depends on the total gravitational potential, which in turn depends on the spatial distribution of each component. We simplify our task by making two assumptions. First, we neglect the contribution by the stellar component to the total gravitational potential throughout most of the paper and return to quantify this effect in Section 5.3. Second, we assume that the DM halo has a fixed form and hence a fixed gravitational potential. We note that this assumption may break down on timescales much longer than a galactic orbital period. We plan to investigate the response of the DM halo in a follow-up study.

The resulting steady-state momentum equation for the gas component in the total gravitational potential of gas and dark matter takes the following form.

$$\frac{1}{\rho_g} \nabla P + (\mathbf{v} \cdot \nabla) \mathbf{v} = \mathbf{g}_g + \mathbf{g}_h, \quad (1)$$

where $P = \rho_g \sigma_g^2$ is the gas pressure, σ_g is the one-dimensional gas velocity dispersion, ρ_g is the gas volume density, \mathbf{v} is the gas velocity, and \mathbf{g}_g and \mathbf{g}_h are the gravitational accelerations due to the gas and DM halo, respectively. The gravitational acceleration \mathbf{g}_g is calculated as $\mathbf{g}_g = -\nabla\Phi$, where the gas gravitational potential Φ is obtained via the solution of the Poisson equation

$$\nabla^2 \Phi = 4\pi G \rho_g. \quad (2)$$

For rotating equilibria, it is most convenient to expand equation (1) in cylindrical coordinates (r, z) with imposed axial symmetry, i.e., $\partial/\partial\phi = 0$. A steady state solution implies that $v_z = 0$ and $v_r = 0$ (but $v_\phi \neq 0$) and the resulting equations are

$$\sigma_g^2 \frac{d \ln \rho_g}{dr} = \frac{v_\phi^2}{r} - \frac{d\sigma_g^2}{dr} + g_{g,r} + g_{h,r} \quad (3)$$

$$\sigma_g^2 \frac{d \ln \rho_g}{dz} = -\frac{d\sigma_g^2}{dz} + g_{g,z} + g_{h,z}. \quad (4)$$

In this study, we assume that the gas temperature is spatially uniform (see Section 3.2), which implies that the spatial derivatives of σ_g^2 are zeroed.

Equations (3) and (4) are discretized using a first-order backward-difference scheme on a cylindrical mesh with 600×600 grid points assuming the axial and midplane symmetry around the z -axis ($r = 0$) and the midplane $z = 0$, respectively. The resulting set of 600^2 linear equations is solved using a forward substitution scheme explained in detail in the Appendix.

3. Initial conditions

3.1. Dark matter halo setup

In order to solve equations (3) and (4) for the gas density ρ_g , one needs to specify the form of the DM halo. We take two distributions that are most often used to fit the rotation curves of

DGs. The first choice is a quasi-isothermal sphere, which has a flat near-central density distribution and a tail inversely proportional to the square of the distance from the galactic center $\varpi = (z^2 + r^2)^{1/2}$ and is described by the following equation

$$\rho_{\text{qis}} = \frac{\rho_0}{1 + (\varpi/r_0)^2}. \quad (5)$$

The central density ρ_0 and the characteristic scale length of the quasi-isothermal halo can be calculated using the following relations (e.g. Mac Low & Ferrara, 1999; Silich & Tenorio-Tagle, 2001)¹

$$r_0 = 0.89 \times 10^{-5} \left(\frac{M_{\text{DM}}}{M_\odot} \right)^{1/2} H^{1/2} \text{ kpc}, \quad (6)$$

$$\rho_0 = 6.3 \times 10^{10} \left(\frac{M_{\text{DM}}}{M_\odot} \right)^{-1/3} H^{-1/3} M_\odot \text{ kpc}^{-3}, \quad (7)$$

where M_{DM} is the mass of the DM halo contained within the virial radius

$$\varpi_{\text{vir}} = 0.016 \left(\frac{M_{\text{DM}}}{M_\odot} \right)^{1/3} H^{-2/3} \text{ kpc}. \quad (8)$$

We note that for a fixed H (set to 0.65 in the current paper for consistency with the work of Mac Low & Ferrara (1999)) the quasi-isothermal halo is uniquely determined by a choice of M_{DM} . Finally, the gravitational acceleration of the quasi-isothermal halo can be written as

$$\mathbf{g}_h = -4\pi G \rho_0 r_0^3 / \varpi^2 [\varpi/r_0 - \arctan(\varpi/r_0)] \mathbf{e}_*, \quad (9)$$

where $\mathbf{e}_* = \varpi/\varpi$ is the unit vector.

The second choice for the form of the DM halo is the well-known NFW density profile suggested by Navarro et al. (1997), which features a cuspy profile in the inner regions and a tail inversely proportional to ϖ^3

$$\rho_{\text{NFW}} = \frac{\rho_c}{(\varpi/r_c)(1 + \varpi/r_c)^2}, \quad (10)$$

where ρ_c and r_c are free parameters. The mass of the DM halo contained within radius ϖ can be expressed as

$$M_{\text{DM}}(\varpi) = \frac{M_{\text{DM}}}{f(c)} \left[\ln(1+x) - \frac{x}{1+x} \right], \quad (11)$$

where $x = \varpi c / \varpi_{\text{vir}}$, $f(c) = \ln(1+c) - c/(1+c)$, c is the concentration parameter, and the virial radius ϖ_{vir} is defined by equation (8). The concentration parameter is determined from the statistics of the Λ CDM halo concentrations by Neto et al. (2007)

$$c = 4.67 \left(\frac{M_{\text{DM}}}{10^{14} M_\odot} H^{-1} \right)^{-0.11}. \quad (12)$$

Finally, the gravitational acceleration due to the NFW halo can be calculated as

$$\mathbf{g}_h = -\frac{GM_{\text{DM}}(\varpi)}{\varpi^2} \mathbf{e}_*. \quad (13)$$

A DM distribution profile, somewhat intermediate between the NFW and the quasi-isothermal profiles, has been semi-empirically introduced by Burkert (1995). It is described by the following equation:

$$\rho_{\text{Burk}} = \frac{\rho_c}{(1 + \varpi/r_c)[1 + (\varpi/r_c)^2]}. \quad (14)$$

¹ We note that Mac Low & Ferrara (1999) have a misprint in their equations which has been corrected in Silich & Tenorio-Tagle (2001).

It is thus a cored profile (as the quasi-isothermal one) which, in analogy to the NFW profile, declines at large radii as ϖ^{-3} . Although this profile fits well the rotation curves of DGs (Burkert, 1995; Salucci & Burkert, 2000), we have not taken it into consideration, because the results adopting this profile are intermediate between the results with a (cuspy) NFW and a (cored) quasi-isothermal profile. As we show in Sect. 5.2, our results depend very little on the DM profile, hence, for the sake of conciseness, we have not considered the Burkert profile.

3.2. The gas temperature

The thermal properties of gas affect the form of the resulting equilibrium configuration. A fully self-consistent approach requires solving for the thermal balance equation along with the steady-state equations (3) and (4). This however entails a considerable increase in calculation time and, sometimes, results in poor convergence.

In this study, we take a simpler approach and build equilibrium configurations for a pre-defined gas temperature. This approach is justified if the characteristic cooling/heating time of gas is much shorter than the dynamical time. The pre-defined gas temperatures are varied in a wide range, starting from 100 K, typical for the cold atomic clouds, to a few $\times 10^4$ K, typical for the warm diffuse gas.

3.3. Rotational versus thermal support

In order to construct rotating equilibria, one needs to specify the form of the rotation curve. A usual approach is to set the rotation velocity of gas v_ϕ to the circular velocity v_{circ} , thus assuming that the support against gravity comes mainly from rotation² (e.g. Mac Low & Ferrara, 1999). Such an assumption taken blindly may produce flattened gaseous disks with *surface* densities nearly independent of galactic radius or even increasing outward, which is unlikely when compared to real systems³.

A more general and realistic approach is to assume that part of the support against gravity comes from pressure gradients and to set $v_\phi = \alpha v_{\text{circ}}$, where α is the spin parameter that determines the relative contribution of rotation to the total support against gravity. For $\alpha = 1$, the gas disk is almost totally supported by rotation, whereas for $\alpha = 0$ the disk is thermally supported. The resulting expression for the rotational velocity of gas is

$$v_\phi = \alpha \left[r \left(|g_{h,r}(z=0)| + |g_{g,r}(z=0)| \right) \right]^{1/2}, \quad (15)$$

where the subscript r denotes the radial component of the gravitational accelerations, the latter being calculated in the midplane $z = 0$ ⁴. This choice makes the rotation velocity z -independent, in concordance with the Poincaré-Wavre theorem (Lebovitz, 1967) for a barotropic gas in rotation equilibrium. More realistic rotating equilibria with a negative vertical gradient of v_ϕ require considering a more general baroclinic gas (Barnabé et al., 2006), which is out of the scope of the present study. Throughout most of the paper, we use $\alpha = 0.9$ (Tomisaka & Ikeuchi, 1988;

² Still there will be some support from gas pressure gradients because circular velocity is not an exact solution of the steady-state equation (1) with $P \neq 0$.

³ As mentioned in the Introduction, it is very likely that the gas vertical scale height naturally increases outward, producing flaring, but the vertically integrated gas volume density (i.e., surface density) decreases outward.

⁴ In practice, we calculate $|g_{h,r}(z=0)|$ and $|g_{g,r}(z=0)|$ in the first layer of computational cells lying right above the midplane.

Strickland & Stevens, 2000) and explore the dependence of our results on smaller values of α in Section 5.1.

3.4. Boundary conditions

The final step is to specify the values of gas volume density ρ_g at the boundaries. We use a computational box with physical dimensions of 8.0 kpc along the r - and z -axes, with the spatial resolution of 13.3 pc along each coordinate direction. Reflecting boundary conditions at the z - and r -axes are a natural choice. In addition, one needs to define the bounding pressure, i.e., the values of ρ_g and σ_g at the outer z - and r -boundaries, if a galaxy is submerged in a dense and hot intra-cluster medium. These values however are essentially free parameters, since they depend on the environment. Hence we decide to take a different approach and define the value of gas number density $n_{0,0}$ in the innermost computational cell near the origin ($z = 0, r = 0$). This value is kept fixed throughout the iterative solution procedure (described below) and serves as a "seed" density needed to solve equations (3) and (4). Increasing/decreasing the value of $n_{0,0}$ would yield more/less massive gaseous disks of different spatial configuration. Thus, at variance with Mac Low & Ferrara (1999), our model galaxies do not have a disk cutoff radius. On the other hand, because of that, ours are truly equilibrium configurations and the disk does not tend to expand into the intracluster medium as in Mac Low & Ferrara (see the test problem in the Appendix).

The choice of α , σ_g and $n_{0,0}$, along with the mean molecular weight $\mu = 1.26$ (for a metallicity of 1/100 that of the solar) and reflecting boundary conditions at the z - and r -axes, completes the initial setup and allow us to calculate equilibrium configurations of gaseous disks for different shapes and masses of the DM halo. The bounding effect of the external environment will be addressed in a future study.

3.5. The solution procedure

One can notice that, since \mathbf{g}_g is obtained through the solution of the Poisson equation (2), equations (3) and (4) are transcendental and hence require an iterative solution procedure described schematically in Fig. 1. The calculation begins with *a*) choosing the DM halo profile (quasi-isothermal sphere or NFW halo), *b*) calculating the corresponding gravitational acceleration \mathbf{g}_h , *c*) fixing the thermal properties of gas, i.e., the gas temperature, and *d*) making an initial guess for the gas volume density $\rho_{g,init}$ and rotational velocity $v_{\phi,init}$. For the former we usually choose a spatially uniform distribution with $\rho_g = m_H \mu n_{0,0}$ and the latter is determined from equation (15). Finally, the gravitational acceleration \mathbf{g}_g of the gas configuration is calculated by solving for the Poisson equation using the alternative direction implicit method as described in Black & Bodenheimer (1975) and Stone & Norman (1992).

The first loop of iterations begins with solving for the steady-state equations (3) and (4). The resulting gas density ρ_g is compared against the initial guess $\rho_{g,init}$ for every computational cell and if the *maximum* relative error ϵ is larger than 10^{-5} , then the iteration cycle repeats by setting $\rho_{g,init} = \rho_g$ and calculating new gravitational potential and rotation curve of the gas disk. Usually, convergence is achieved after 10–15 iterations, but may sometime diverge signaling for an inappropriate initial guess for $n_{0,0}$ or α , especially when $n_{0,0}$ is large and the corresponding equilibrium solution near the rotation axis is characterized by a

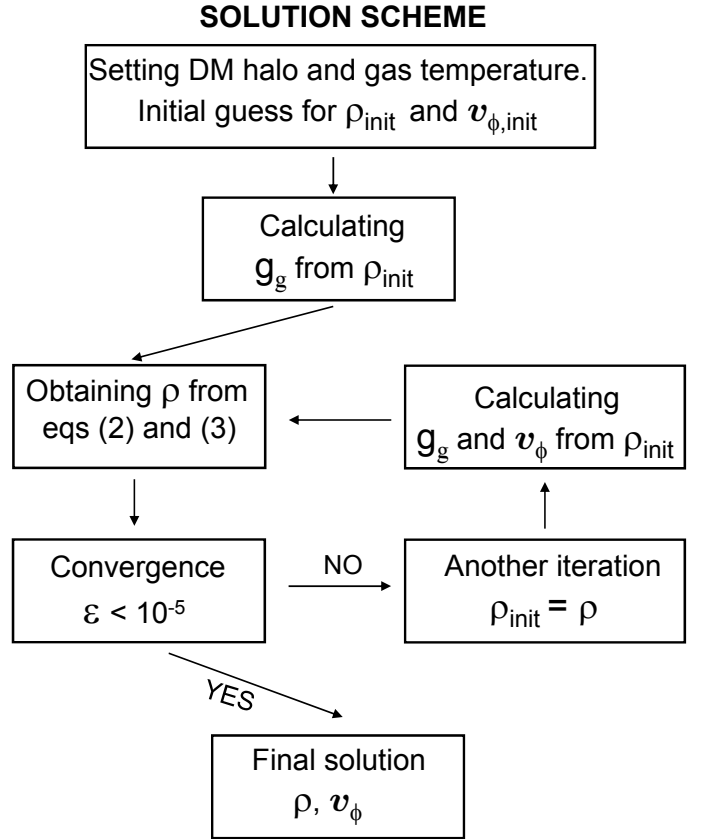


Fig. 1. Schematic representation of the iterative solution procedure to calculate rotating, self-gravitating gaseous equilibria in DM halos.

narrow, high-density plateau which is difficult to resolve numerically.

4. Self-gravitating equilibrium gaseous disks

4.1. Star formation criteria

We build equilibrium gaseous disks hosted by DM halos of various mass and shape and determine the minimum gas mass needed to trigger star formation in these systems. Three criteria are employed to assess the feasibility of star formation in our model galaxies. The first criterion is based on theoretical considerations of gravitational stability in self-gravitating systems. We assume that star formation is allowed if the Toomre Q parameter

$$Q_T = \frac{v\sigma_g}{\pi G \Sigma} \quad (16)$$

is smaller than a critical value Q_c , where v is the epicycle frequency and Σ is the gas surface density. The classical analysis of thin, axisymmetric gaseous disks suggests a value of $Q_c = 1.0$ (Toomre, 1964), but Q_c in real systems is usually somewhat greater and may depend on many factors including the galaxy class, the form of the rotation curve, the disk thickness, the strength of magnetic fields, etc (e.g. Polyachenko et al., 1997; Kim & Ostriker, 2001; Bigiel et al., 2008; Leroy et al., 2008; Dong et al., 2008; Roychowdhury et al., 2009). In this study, we take a conservative value of $Q_c = 2.0$ and assume that our model galaxy is prone to star formation if $Q_T < Q_c$ in at least some parts of the gas disk.

For the second star formation criterion, we make use of empirical studies of star formation in the Local Universe by

Table 1. Quasi-isothermal DM halo parameters

$M_{\text{DM}} (M_{\odot})$	r_0 (kpc)	$\rho_0 (M_{\odot} \text{ pc}^{-3})$	ϖ_{vir} (kpc)
10^7	2.27×10^{-2}	0.337	4.6
10^8	7.2×10^{-2}	0.157	9.9
10^9	0.23	0.073	21.3
10^{10}	0.72	0.034	45.9

Kennicutt (1998, 2008) who compares disk-averaged star formation (rates per unit area) versus gas surface densities in normal and starburst galaxies, including DGs. These studies suggest the following scaling law (hereafter, the Kennicutt-Schmidt law) between the star formation rate per unit area $\Sigma_{\text{SFR}} (M_{\odot} \text{ yr}^{-1} \text{ kpc}^{-2})$ and the gas surface density $\Sigma (M_{\odot} \text{ pc}^{-2})$

$$\Sigma_{\text{SFR}} = (2.5 \pm 0.7) \times 10^{-4} \left(\frac{\Sigma}{1 M_{\odot} \text{ pc}^{-2}} \right)^{1.4 \pm 0.15}, \quad (17)$$

with a threshold density Σ_c of the order of $5.0 M_{\odot} \text{ pc}^{-2}$, below which very rare cases of large-scale star formation are detected. Therefore, we use this value as the second star formation criterion and assume that star formation can be triggered in our model galaxies if $\Sigma > \Sigma_c$.

So far, we have used vertically integrated gas densities to assess the model's susceptibility to star formation. However, star formation recipes may also rely on the critical gas *volume* density n_c , as is often done in numerical hydrodynamics simulations. Moreover, as discussed in Elmegreen (1997), a Schmidt law with index 1.5 would be expected for self-gravitating disks, if the SF rate is equal to the ratio of the local gas volume density to the free-fall time, all multiplied by some efficiency. The adopted values of n_c vary in wide limits, depending on the numerical resolution but most studies use values of the order of $0.1\text{--}1.0 \text{ cm}^{-3}$ (e.g. Springel & Hernquist, 2003; Schaye & Dalla Vecchia, 2008), though some authors adopt much higher values (e.g. Tasker, 2011).

In this paper, we assume that SF is allowed if there is enough gas mass (in the vertical column that fulfils the first two criteria) with number density n_g greater than a fiducial critical value of $n_c = 1.0 \text{ cm}^{-3}$ to allow for a SF event of non-negligible magnitude, i.e., if

$$M_{\text{g}}^{\text{SF}} (n_g \geq 1.0 \text{ cm}^{-3}) > 10^4 M_{\odot}. \quad (18)$$

We choose to set a limit in mass rather than in size because star formation may be localized to just a few tens of parsec, yet contain enough gas mass for a star formation event of notable magnitude. Finally, a model galaxy is assumed to be prone to star formation only if all three criteria are satisfied altogether.

4.2. Equilibrium models

Throughout most of the paper, we use a quasi-isothermal DM halo with four different masses $M_{\text{DM}} = 10^7 M_{\odot}$, $10^8 M_{\odot}$, $10^9 M_{\odot}$, and $10^{10} M_{\odot}$. The corresponding values for r_0 , ρ_0 , and ϖ are listed in Table 1. We set the gas spin parameter to $\alpha = 0.9$ and the gas temperature T_g to a *spatially* uniform value that is either independent of the halo mass ($T_g = 10^4 \text{ K}$) or scales with the DM mass as $T_g \propto M_{\text{DM}}^{2/3}$, as suggested by the virial relations. We consider the effect of varying rotational support against gravity (i.e., varying α) in Section 5.1, the effect of a different DM halo configuration (i.e., the NFW halo) in Section 5.2, and the effect of non-negligible stellar disk in Section 5.3.

To put things in the physical context, the models considered here and in Sections 5–5.2 (with a gas distribution in equilibrium with a DM halo, waiting for the onset of star formation) can be considered as progenitors of, e.g., Blue Compact Dwarf galaxies whose stellar populations are largely dominated by very young stars (Papaderos et al., 2008). In Section 5.3 we describe objects with a pre-existing disk of stars which have smoothly accreted gas and have achieved a new equilibrium configuration (galaxies surrounded by extended gas reservoirs are quite common (see e.g. van Zee et al., 1998, for the case of I Zw 18)). Finally, in Section 5.4 we assume a redshift of galaxy formation significantly larger than zero. Therefore, our equilibrium configurations should be treated as proxies to DGs that have built up their gas mass reservoir by a quasi-steady accretion or have temporarily achieved a quasi-steady state after an episode of fast accretion.

Figure 2 presents gas surface densities Σ (left column), Toomre Q parameters (middle column), and gas rotation velocities v_{ϕ} (right column) for various steady-state gaseous disks with M_{DM} ranging from $10^{10} M_{\odot}$ (top row) to $10^7 M_{\odot}$ (bottom row). The spin parameter and the spatially constant gas temperature are the same for all models and are equal to 0.9 and 10^4 K , respectively. In the calculation of the Q parameter and v_{ϕ} we use mass-weighting according to the gas mass contained in every computational cell. The gas surface density is obtained by integrating ρ_g along the z -axis.

For each value of M_{DM} , we consider five models with different seed values of the gas number density $n_{0,0}$, namely, 0.01, 0.1, 1.0, 5.0, and 25 cm^{-3} . These models are distinguished in Figure 2 by lines of different style, with the dotted lines corresponding to $n_{0,0} = 0.01 \text{ cm}^{-3}$ and dashed lines to $n_{0,0} = 25 \text{ cm}^{-3}$ (and the other models in between in the order of increasing $n_{0,0}$). The largest/smallest values of $n_{0,0}$ produce models with highest/lowest gas surface densities near the galactic center.

The radial profiles of Σ in Figure 2 indicate that models with lower values of M_{DM} produce less centrally concentrated gaseous distributions. Indeed, models with $M_{\text{DM}} = 10^{10} M_{\odot}$ have a density tail proportional to r^{-2} , whereas models with $M_{\text{DM}} \leq 10^8 M_{\odot}$ are characterized by $\Sigma \propto r^{-1.1}$. This tendency can be explained by the fact that the mass of the gas disk starts to systematically exceed that of the DM halo for $M_{\text{DM}} \leq 10^9 M_{\odot}$, the effect discussed in more detail in Section 5. As a result, the shape of the gas disk in models with $M_{\text{DM}} \leq 10^9 M_{\odot}$ is mostly determined by self-gravity of the gas, with the resulting distribution approaching that of a self-gravitating isothermal ellipsoid with the density tail $\rho_g \propto \varpi^{-2}$ or $\Sigma \propto r^{-1}$. We also note that models with lowest values of Σ tend to have surface density profiles independent of radius.

For a given DM halo mass and equal gas temperature, models with lower values of Σ have higher values of the Q parameter, as expected. It is worth noting that the lowest Q_{T} is often found a few hundred or even thousand parsecs away from the galactic center. This behaviour can be understood by analysing the radial dependence of the epicycle frequency $\nu = (4\Omega^2 + r d\Omega^2/dr)^{1/2}$. This quantity is independent of radius r in the inner parts $r \ll r_0$, where the DM halo and gas densities are nearly constant and $\Omega \approx \text{const}$. On the other hand, at $r \gg r_0$ the epicycle frequency declines with radius because the DM halo and gas densities also (as a rule) decline with radius. This implies that Q_{T} is nearly independent of r in the inner parts but may increase or decrease in the outer parts depending on the radial profile of the gas surface density Σ . For models with Σ nearly independent of radius, Q_{T} generally decreases at large radii (because ν also decreases but other quantities stay nearly constant), whereas for models show-

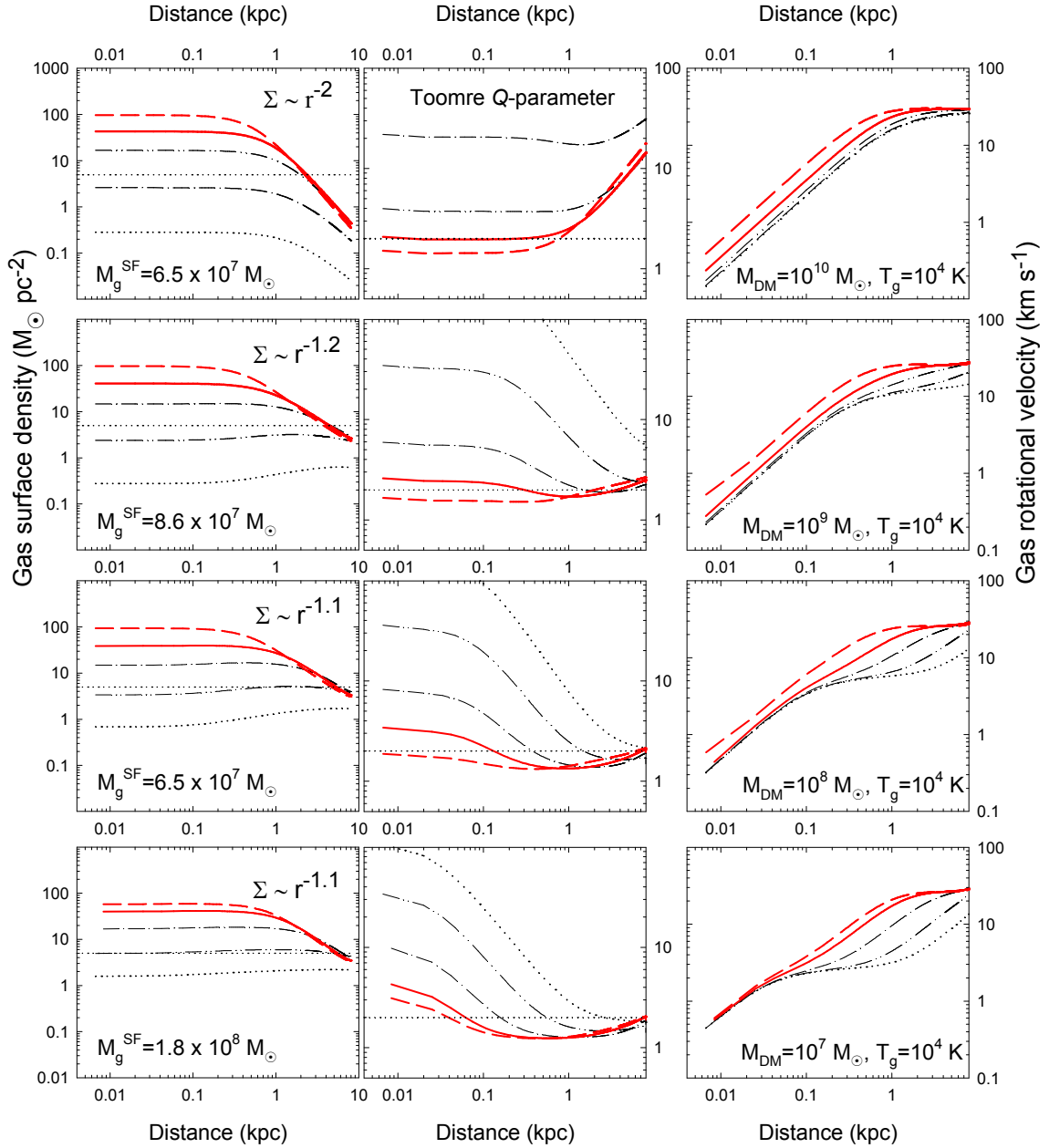


Fig. 2. Gas surface densities (left column), Toomre Q parameters (middle column), and rotation velocities (right column) of self-gravitating (steady-state) gaseous disk hosted by quasi-isothermal DM halos with four masses M_{DM} as indicated in the right column. The spatially uniform gas temperature and the spin parameter are set to $T_g = 10^4$ K and $\alpha = 0.9$, respectively. The horizontal dotted lines mark the adopted critical surface density for star formation $\Sigma_c = 5 M_{\odot} \text{ pc}^2$ (left column) and the critical Toomre parameter Q_{cr} for gravitational stability (middle column). For every value of M_{DM} , five models with different values of the seed density $n_{0,0} = 25.0, 5.0, 1.0, 0.1,$ and 0.01 cm^{-3} from the uppermost to the lowermost line are considered. Greater $n_{0,0}$ produce models with higher gas surface densities in the inner regions. The models that are susceptible to star formation according to the adopted star formation criteria are marked with red thick lines and the gas mass M_{g}^{SF} with number density greater than a critical value of 1.0 cm^{-3} is indicated in the left column for models plotted with solid red lines.

ing a decline in Σ at large radii, the corresponding values of Q_{T} attain a minimum at some several hundred or thousand parsecs and increases on both sides.

It is also worth noting that the rotation curves of our model galaxies either steadily rise or flatten out only at large radii. This behaviour is in qualitative agreement with the observed rotation curves of DGs (see e.g. de Blok et al., 2008; Oh et al., 2008; Swaters et al., 2009, 2011).

The horizontal dotted lines in the left and middle columns of Fig. 2 mark the critical gas surface density for star formation $\Sigma_c = 5 M_{\odot} \text{ pc}^2$ and the critical Toomre parameter $Q_c = 2.0$. We use these values to determine models that can allow for star formation, i.e., models for which both criteria $\Sigma > \Sigma_c$ and $Q_{\text{T}} < Q_c$ are met at least in some parts of the galactic disk, and also the gas mass M_{g}^{SF} with number density greater than 1.0 cm^{-3} exceeds a minimum value of $10^4 M_{\odot}$ as stipulated by the third SF condi-

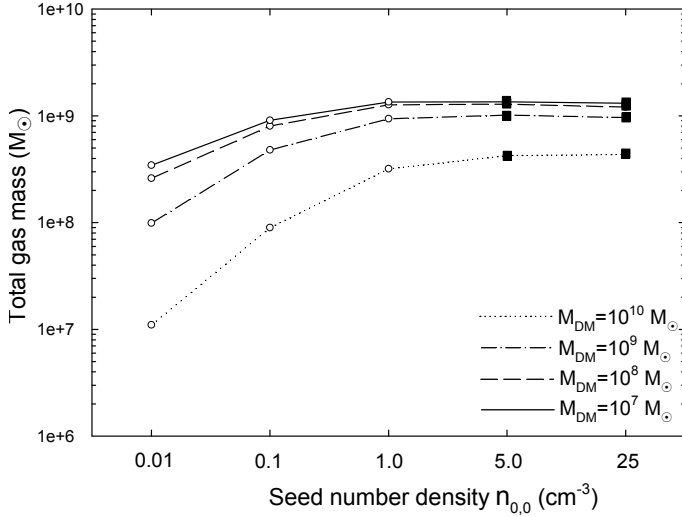


Fig. 3. Total gas masses M_g calculated for five models with different seed density values $n_{0,0}$. The filled squares mark the models that are susceptible to star formation according to the adopted criteria. Lines of different style connect models with equal masses of the DM halo.

tion. Such “star-formation-allowed” models are highlighted with red color in Fig. 2.

For every model in Figure 2, we calculate the total gas mass M_g contained within our computational domain, the latter having a cylindrical shape with radius of 8 kpc and height of 8 kpc on both sides from the midplane. We use M_g as a proxy for the total gas mass⁵, and estimate the possible missing gas mass using the surface density profiles in Fig. 2. For models with $M_{DM} = 10^{10} M_\odot$, $\Sigma(r) \propto r^{-2}$ and $M_g(r) \propto \ln(r)$ at large radii, implying a small correction of order unity for a computational box with size three times greater than ours (24×24 kpc). For models with $M_{DM} \leq 10^8 M_\odot$, $\Sigma(r) \propto r^{-1.1}$ and $M_g(r) \propto r^{0.9}$, implying a factor of 2.7 increase in the total gas mass. This means that our estimates are accurate to within a factor of unity for models with $M_{DM} \gtrsim 10^9 M_\odot$, while for models with smaller DM halos we may underestimate the total gas mass by up to a factor of 3.

The total gas masses M_g for every model are plotted in Fig. 3. The bottom axis shows the seed number density $n_{0,0}$ for each model. Lines of different style connect models with the same mass of the DM halo (e.g., models with $M_{DM} = 10^9 M_\odot$ are connected with the dash-dotted line). We distinguish the star-formation-allowed models by the filled squares.

It is evident that DM halos can host steady-state gaseous disks with various masses, but not all gas configurations are prone to star formation. There exists a minimum gas mass M_g^{\min} that a DM halo needs to accumulate in order to fulfil the star formation criteria. For instance, for a DM halo with mass $10^{10} M_\odot$ (dotted line) the corresponding minimum gas mass is $4.3 \times 10^8 M_\odot$, while for a DM halo with mass $10^8 M_\odot$ (dashed line) the corresponding minimum gas mass is $1.3 \times 10^9 M_\odot$. As one can see, M_g^{\min} depends on the mass of the DM halo and may increase as M_{DM} decreases. The latter effect is not unexpected – a DM halo with smaller mass has a weaker gravitational potential and, as a consequence, a more massive gaseous disk is required to attain the critical density for star formation. The gas

self-gravity here is a key factor, without which such an effect will be absent.

5. Minimum gas mass for star formation vs. dark matter halo mass

In this section, we study in more detail the dependence of the minimum gas mass for star formation M_g^{\min} on the mass of the DM halo, as well as on other properties of galactic systems. We want to emphasize here that M_g^{\min} is the total gas mass of a galaxy in which star formation is allowed according to the adopted SF criteria and not the gas mass M_g^{SF} that fulfils the star formation criterion (18). The latter quantity is always smaller than M_g^{\min} as only part of the gas disk is characterized by $n_g > n_c$. We choose to concentrate on M_g^{\min} because we compare this quantity to the baryonic mass derived from the Λ CDM theory.

Throughout the paper we consider quasi-isothermal DM halos (if not specified otherwise) described by equations (5)–(8). The top panel in Figure 4 presents the M_g^{\min} – M_{DM} relation for the four values of the DM halo mass ($10^7 M_\odot$, $10^8 M_\odot$, $10^9 M_\odot$, and $10^{10} M_\odot$). In particular, the thick blue solid line shows the data for the spin parameter $\alpha = 0.9$ and gas temperature $T_g = 10^4$ K (independent of the DM halo mass), whereas the thick blue dashed line does that for $T_g \propto M_{DM}^{2/3}$ and the same value of α^6 . The latter relation is normalized to $T_g = 10^4$ K for $M_{DM} = 10^{10} M_\odot$, which yields the following scaling law

$$T_g = 2.15 \times 10^{-3} M_{DM}^{2/3}. \quad (19)$$

The corresponding values of T_g are indicated in Fig. 4 for every pair of data (M_g^{\min} , M_{DM}). The adopted set of parameters (quasi-isothermal DM halo, $\alpha = 0.9$, and gas temperature either dependent on or independent of M_{DM}) is denoted hereafter as the reference model. The bottom panel in Figure 4 also shows the ratio $\xi = M_g^{\min}/M_{DM}$ versus M_{DM} .

The dotted line in Figure 4 presents the baryonic mass M_b for a given DM halo mass as expected from the Λ CDM theory and WMAP4 data (Spergel et al., 2003) with $\Omega_b/\Omega_m = 0.17$. If we treat M_b as an *upper* limit of the available gas mass, it becomes evident that galaxies with $M_{DM} \leq 10^9$ and $T_g = 10^4$ K require much more gas than available to achieve a state in which star formation is allowed. This statement applies to quasi-steady systems and may break down for galaxies that accumulate their gas mass reservoir via a series of violent mergers or if an external perturbation drives the system out of equilibrium and triggers star formation in some parts of the galaxy, as discussed later in Section 8.1.

An alternative solution is that galaxies can cool to sufficiently low temperatures to warrant a more compact and dense gas configuration. Figure 5 shows gas surface densities Σ (left column), Toomre Q parameters (middle column), and gas rotation velocities v_ϕ (right column) for the same parameters as in Figure 2 but for $T_g \propto M_{DM}^{2/3}$ as described by eq. (19), with the corresponding gas temperatures indicated for every M_{DM} in the right column. One can see that the gas surface density profiles are considerably steeper for cooler gas disks and are characterized by approximately the same power law r^{-2} in the outer regions. Furthermore, the transition radius from a near-constant surface density to the sloped one decreases with mass⁷, in con-

⁵ We cannot extend our computational boundaries to a distance much greater than 8 kpc because of the need for high spatial resolution to resolve the inner density plateau.

⁶ We remind that in all models the gas temperature is spatially uniform but its value may or may not depend on M_{DM} .

⁷ Diminishing pressure support against gravity in models with smaller T_g is compensated by an increase in the gas density slope.

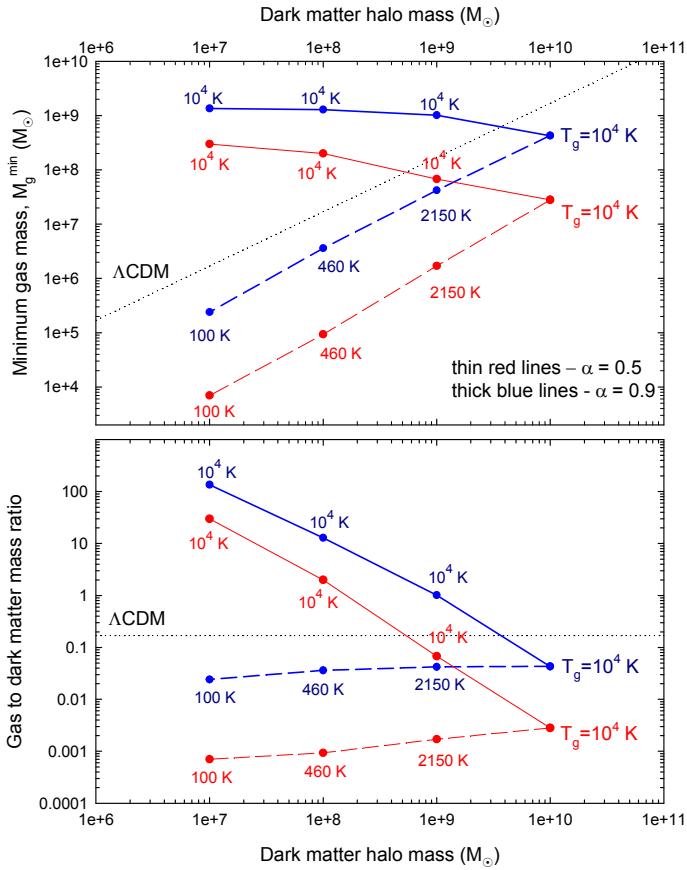


Fig. 4. Top. Minimum gas mass for star formation M_g^{\min} as a function of the DM halo mass M_{DM} . The thick blue lines show the data for the reference model (quasi-isothermal DM halo, spatially uniform T_g , and $\alpha = 0.9$), while the thin red lines show the effect of a smaller spin parameter $\alpha = 0.5$. The solid lines (of corresponding color) refer to models with $T_g = 10^4$ K, while the dashed lines show models with gas temperature according to eq. (19). Numbers denote the corresponding gas temperatures for every model. The dotted line gives the available baryonic mass M_b as suggested by the Λ CDM theory with $\Omega_b/\Omega_m = 0.17$. **Bottom.** Ratio M_g^{\min}/M_{DM} versus M_{DM} for the same models as in the top panel.

trast to models with the DM-mass-independent gas temperature T_g (Fig. 2).

The star formation criteria (16) and (17) are satisfied only in the inner parts of our model galaxies, with the size of the star formation region shrinking to a few tens of parsecs for models with $M_{\text{DM}} \leq 10^8 M_\odot$. Moreover, the value of M_g^{SF} notably decreases for lower mass DM halos. These very compact starburst regions are not unusual in low mass star forming galaxies. For instance, the galaxy SBS 0335-052 has a star forming radius of only ~ 20 pc (see e.g. Takeuchi et al., 2003).

As the blue dashed line in the top panel of Fig. 4 demonstrates, models with $T_g \propto M_{\text{DM}}^{2/3}$ have much smaller M_g^{\min} than models with $T_g = 10^4$ K. Moreover, models with $T_g \propto M_{\text{DM}}^{2/3}$ are characterized by $M_g^{\min} < M_b$, meaning that such galaxies may have enough gas reservoir to achieve a state in which SF is allowed. However, the required gas temperatures are quite low, especially for $M_{\text{DM}} \leq 10^8 M_\odot$. Moreover, the obtained rotation curves (third column in Figure 5) are much flatter for models with $M_{\text{DM}} \leq 10^8 M_\odot$ than for their more massive counterparts.

We conclude that models with $T_g \propto M_{\text{DM}}^{2/3}$ can provide a better agreement with the Λ CDM predictions but at the cost of a worsening agreement with observations for the low DM mass models.

5.1. The effect of varying rotation support

Decreasing the amount of rotation leads to more compact and dense gas configurations as the pressure forces start to play an ever increasing role in the support against gravity. Therefore, one can expect that lowering the spin parameter would produce steady-state gaseous configurations with steeper gas surface density profiles (provided that the gas temperature is constant).

This effect is illustrated in Figure 6 showing the gas surface density distributions for models with $\alpha = 0.5$ (solid lines) and $\alpha = 0.9$ (dashed lines). For the sake of convenience, we compare only the star-formation-allowed models⁸ with the smallest value of M_g^{\min} . In the case of $\alpha = 0.9$, such models are distinguished by red solid lines in Figures 2 and 5. As one can see, models with smaller α are characterized by more compact gas disks with steeper density profiles at large radii. This effect takes place because the $\alpha = 0.5$ models compensate for a smaller rotation support with steeper gas density (and pressure) gradients. As a result, these models also have smaller M_g^{SF} than the corresponding $\alpha = 0.9$ models⁹.

Figure 4 illustrates the effect of a smaller rotation support against gravity. The thin red lines show the data for $\alpha = 0.5$, with other parameters being identical to those of the reference model. It is evident that the minimum gas mass for star formation M_g^{\min} is substantially lower in galaxies with smaller values of α . The effect is particularly strong for galaxies with $T_g \propto M_{\text{DM}}^{2/3}$. Lowering further the spin parameter to $\alpha = 0.25$ yields only a factor of two decrease in M_g^{\min} at most. We point out that the minimum gas mass for star formation M_g^{\min} remains still much greater than the available baryonic mass M_b for galaxies with $M_{\text{DM}} \leq 10^8 M_\odot$ and $T_g = 10^4$ K.

5.2. Variations in the DM halo form

As already mentioned, the mass and shape of DM halos in DGs are still very uncertain and the problem is highly debated in the literature. If the DM density at small galactocentric radii ϖ is approximated by a power law ($\rho_{\text{DM}} \propto \varpi^{-\beta}$), a value of β close to or slightly smaller than one (i.e., cusps) is obtained in numerical simulations based on the Λ CDM theory (Navarro et al., 1997, 2010). On the other hand, observations suggest values of β close to zero, implying the presence of cores with near-constant DM density at small ϖ (de Blok et al., 2001; Spekkens et al., 2005). This unsolved mismatch between observations and models is commonly referred to as the ‘‘cusp-core problem’’.

Our reference quasi-isothermal DM halos are cored DM profiles. In this section we estimate the effect that a cuspy DM

⁸ Strictly speaking, the $M_{\text{DM}} = 10^7 M_\odot$ and $T_g = 10^2$ K case has no star-formation-allowed models since the third criterion, i.e., $M_g^{\text{SF}} > 10^4 M_\odot$ is not fulfilled even for the highest $n_{0,0}$ model. We relax this requirement in this particular case since the other two SF criteria are nevertheless satisfied.

⁹ We note that some of the $\alpha = 0.5$ models have higher gas densities in the innermost regions, which is the result of a rather coarse grid of models considered in the paper. Nevertheless, the size of this region is rather small (~ 0.2 kpc) and most of the gas mass is still concentrated at large radii.

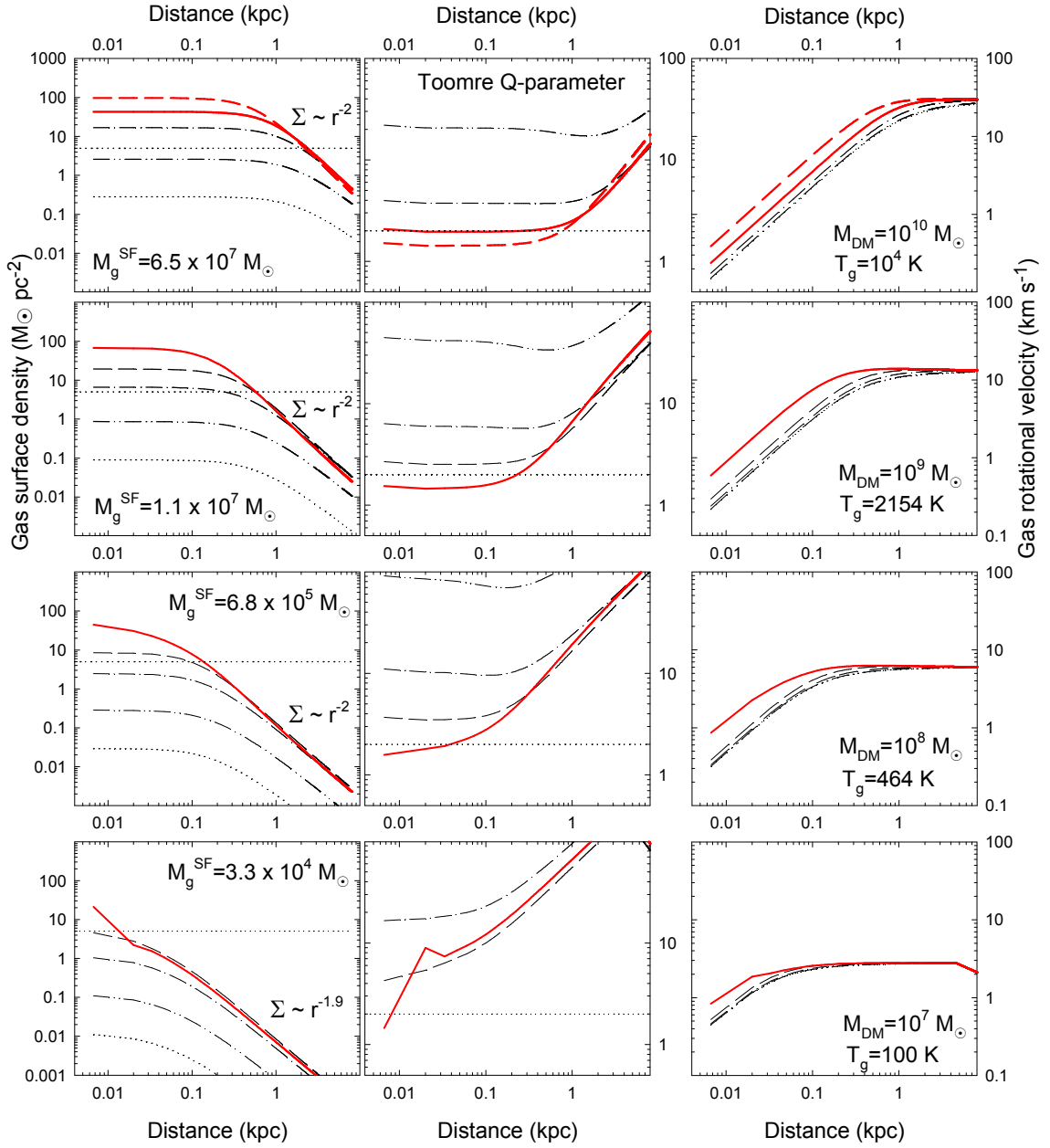


Fig. 5. Same as Fig. 2 only for the gas temperature $T_g \propto M_{\text{DM}}^{2/3}$, with the actual values of T_g indicated in the right column.

halo advocated by Navarro et al. (1997) and described by equations (10)–(12) may have on the values of M_g^{min} . Figure 7 compares the minimum gas masses M_g^{min} obtained in the reference model for the quasi-isothermal DM halo (blue lines) with those calculated for the NFW halo (red lines). As one can see, the difference is negligible for models with $T_g = 10^4$ K and is minimal for models with $T_g \propto M_{\text{DM}}^{2/3}$. Therefore, the form of the DM halo is not expected to play a significant role in determining the minimum gas mass for star formation as far as the total mass of the DM halo is the same.

5.3. The effect of pre-existing stellar disk

So far we have considered model galaxies that consist of a gaseous disk and DM halo. However, real star-forming galaxies in the Local Universe almost always have a pre-existing stellar disk, which may affect the form of the gaseous disk via the stellar

gravitational potential. To explore the extent of this effect, we assume that our galaxies in the reference model have a burst of star formation that turns 10% of the gas content into stars. Star formation takes place in parts of the gas disk that obey the three criteria for star formation $\Sigma > \Sigma_c = 5 M_\odot \text{pc}^{-2}$ and $Q_T < Q_{\text{cr}} = 2.0$. We then construct a new equilibrium gas disk in the combined gravitational potential of gas, stars, and DM halo. The spin parameter of the stellar disk is assumed to be equal to that of the gaseous disk. This assumption is justified if the gas sound speed is comparable to the stellar velocity dispersion, which is often true for DGs.

The black lines in Figure 7 show the minimum gas mass M_g^{min} for new models that take into account a recent burst of star formation. It is evident that the stellar disk has little effect on the value of M_g^{min} irrespective of the DM halo mass (the black line is almost indistinguishable from the blue line showing the reference model). This is explained by the fact that the mass of the stellar disk M_s is only a small addition to the total

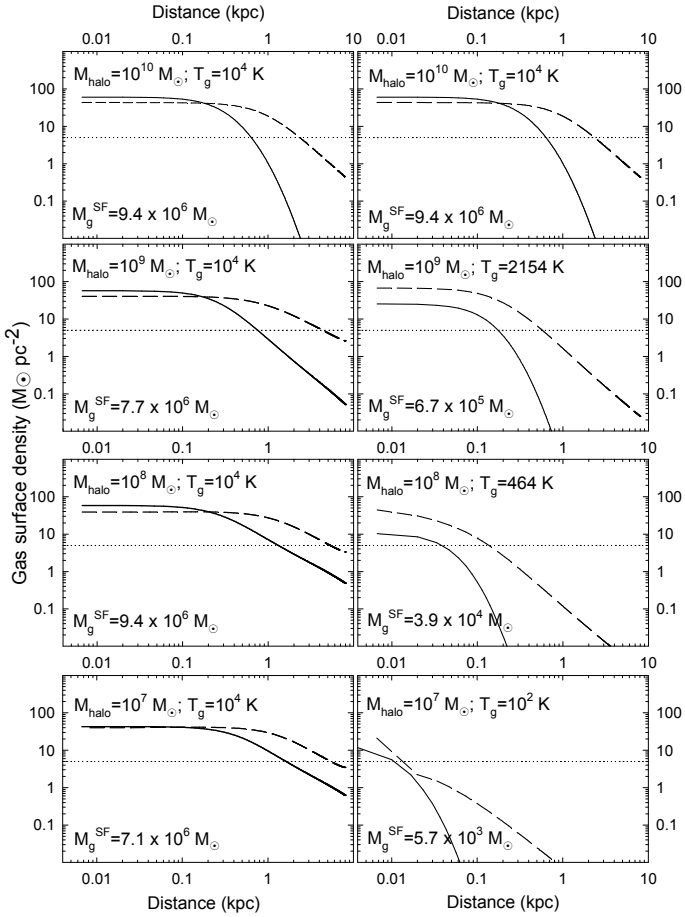


Fig. 6. Comparison of the gas surface density profiles for models with the spin parameter $\alpha = 0.5$ (solid lines) and $\alpha = 0.9$ (dashed lines). The DM halo mass M_{DM} and the gas temperature T_g are indicated in every panel. The gas mass M_g^{SF} with number density greater than 1.0 cm^{-3} is given only for the $\alpha = 0.5$ models.

mass budget. For instance, in models with $M_{\text{DM}} = 10^{10} M_{\odot}$, $M_s = 0.07 M_g^{\text{min}}$ and $M_s = 0.0028 M_{\text{DM}}$. In models with $M_{\text{DM}} = 10^7 M_{\odot}$, $M_s = 0.047 M_g^{\text{min}}$ and $M_s = 4.1 M_{\text{DM}}$ (in both cases, $T_g = 10^4 \text{ K}$). Unless many repetitive bursts of star formation take place with the integrated star formation efficiency considerably exceeding 0.1 (leading to a significant increase in the star to gas mass ratio), we do not expect the gravitational potential of the stellar disk to affect our results. However, we should note that the stellar feedback may drive the gas disk out of equilibrium, thus affecting our estimates of M_g^{min} .

5.4. Galaxies at higher redshifts

In this section, we study the dependence of M_g^{min} on the redshift of galaxy formation z_{gf} . DM halos of the same mass at larger redshifts are more compact and one may expect that this could affect the shape of the gas disk and hence the value of M_g^{min} . We modify equations (6)-(8) to include the dependence on z_{gf} (e.g. Fujita et al., 2003)

$$r_0(z_{\text{gf}}) = r_0 \left(\frac{\Omega_0}{\Omega(z_{\text{gf}})} \right)^{-1/3} (1 + z_{\text{gf}})^{-1} \text{ kpc}, \quad (20)$$

$$\rho_0(z_{\text{gf}}) = \rho_0 \left(\frac{\Omega_0}{\Omega(z_{\text{gf}})} \right) (1 + z_{\text{gf}})^3 M_{\odot} \text{ kpc}^{-3}, \quad (21)$$

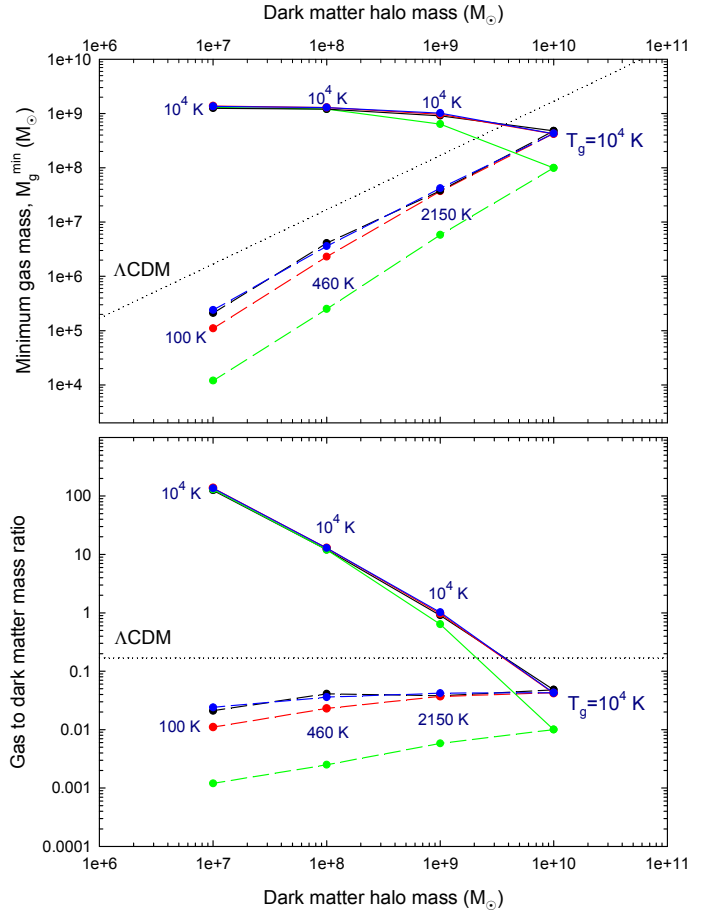


Fig. 7. Top. Minimum gas mass for star formation M_g^{min} versus DM halo mass M_{DM} for the reference model (blue lines), models with a cuspy DM halo (red lines), models with pre-existing stellar disk (black lines), and models at redshift $z_{\text{gf}} = 2.0$ (green lines). The solid lines show models with the gas temperature $T_g = 10^4 \text{ K}$, whereas dashed lines do that for models with $T_g \propto M_{\text{DM}}^{2/3}$ (see equation 19). Numbers indicate the corresponding gas temperatures for every model. The dotted line plots the cosmological relation between the baryonic and DM mass as suggested by the Λ CDM theory. **Bottom.** The corresponding $M_g^{\text{min}}/M_{\text{DM}}$ versus M_{DM} relations.

$$\varpi_{\text{vir}}(z_{\text{gf}}) = \varpi_{\text{vir}} \left(\frac{\Omega_0}{\Omega(z_{\text{gf}})} \right)^{-1/3} (1 + z_{\text{gf}})^{-1} \text{ kpc}, \quad (22)$$

where $\Omega_0 \equiv \Omega(z_{\text{gf}} = 0)$ and $\Omega(z_{\text{gf}})$ is defined as

$$\Omega(z_{\text{gf}}) = \frac{\Omega_m(1 + z_{\text{gf}})^3}{\Omega_m(1 + z_{\text{gf}})^3 + \Omega_{\Lambda}}, \quad (23)$$

with Ω_m and Ω_{Λ} set to 0.24 and 0.76, respectively.

The green lines in the upper panel of Figure 7 show the minimum gas mass for star formation M_g^{min} as a function of M_{DM} in the reference model but with $z_{\text{gf}} = 2.0$. In compliance with the downsizing, low-mass galaxies have a median redshift of star formation smaller than large objects and a value of $z_{\text{gf}} = 2$ well represents an average galaxy formation redshift for DGs (see e.g. Thomas et al., 2005; Cattaneo et al., 2011). We also note that $z_{\text{gf}} = 2.0$ yields roughly a factor of two more compact and a factor of seven denser DM halos.

As one can see, the effect of a higher redshift is quite pronounced for models with $T_g \propto M_{\text{DM}}^{2/3}$ (shown by the green dashed

lines), producing almost a factor of 10 lower values of M_g^{\min} than in the reference model (blue dashed lines). However, for models with $T_g = 10^4$ K, the resulting values of M_g^{\min} quickly approach those of the $z_{\text{gf}} = 0$ models (blue lines) for low values of M_{DM} .

The lowering of M_g^{\min} can be understood if we compare the radial density profiles of the DM halos of equal mass at different redshifts. The right panel in Figure 8 presents the volume density ρ_{qis} of the quasi-isothermal DM halo as a function of radial distance ϖ for the reference model ($z_{\text{gf}} = 0$, dashed lines) and the $z_{\text{gf}} = 2.0$ model (solid lines). The corresponding masses of the DM halos are indicated in each panel. One can see that the DM halos at $z_{\text{gf}} = 2.0$ are characterized by higher densities than their $z_{\text{gf}} = 0$ counterparts. This causes gaseous disks at higher redshifts to assume steeper density profiles to compensate an increasing gravity force of the DM halo. This effect is illustrated in the left panel of Figure 8, which compares the gas surface density profiles in the star-formation-allowed models at $z_{\text{gf}} = 0$ (dashed lines) and the $z_{\text{gf}} = 2.0$ model (solid lines). All other model parameters are those of the reference model and the gas temperature is indicated in each panel. Indeed, the $z_{\text{gf}} = 2.0$ models are characterized by significantly more compact gaseous disks than their $z_{\text{gf}} = 0$ counterparts, which results in systematically lower values of M_g^{\min} .

6. Reconciling the gas to DM ratio with the Λ CDM predictions

Figures 4 and 7 demonstrate that the minimum gas mass for star formation M_g^{\min} may greatly exceed the DM halo mass (and, of course, the gas to DM mass ratio can be largely above the suggested cosmological value of 0.17) for models with $M_{\text{DM}} \leq 10^9 M_\odot$ and $T_g = 10^4$ K. This apparent contradiction between the baryon-to-DM ratios deduced by our models and the cosmologically inferred one should not be a major source of concern at the present stage. In fact, we know already that some objects in the Universe do have baryon-to-DM ratios larger than 0.17 (e.g., globular clusters, high velocity clouds, and probably also dEs and dIrrs, see the Introduction). At the same time, Figures 4 and 7 show that models in which $T_g \propto M_{\text{DM}}^{2/3}$ (as suggested by the virial relations) neatly reproduce a constant gas to DM mass ratio, although below the cosmological value of 0.17.

In this section, we explore whether the cosmological value can be reproduced by our models with either a different choice of the zero point of the T_g – M_{DM} relation or by introducing some non-thermal support against gravity in equation (1). To explore the first possibility, we choose the following scaling law between the gas temperature and the DM halo mass

$$T_g = 4.8 \times 10^{-3} M_{\text{DM}}^{2/3}, \quad (24)$$

which yields roughly a factor of two higher gas temperatures than equation (19), i.e., $T_g = 2.23 \times 10^4$ K for $M_{\text{DM}} = 10^{10} M_\odot$, $T_g = 0.48 \times 10^4$ K for $M_{\text{DM}} = 10^9 M_\odot$, $T_g = 1.03 \times 10^3$ K for $M_{\text{DM}} = 10^8 M_\odot$, and $T_g = 223$ K for $M_{\text{DM}} = 10^7 M_\odot$.

The top panel in Figure 9 shows the minimum gas mass for star formation M_g^{\min} as a function of the DM halo mass M_{DM} . The dashed line presents the data for the new scaling law described by equation (24), while the solid line does that for the old scaling given by equation (19). As one can see, the new scaling law yields somewhat higher gas masses than a cosmological value and the slope of the model M_g^{\min} – M_{DM} relation is somewhat shallower than the cosmological one (dotted line). On the other hand, the old scaling law yields M_g^{\min} that are somewhat

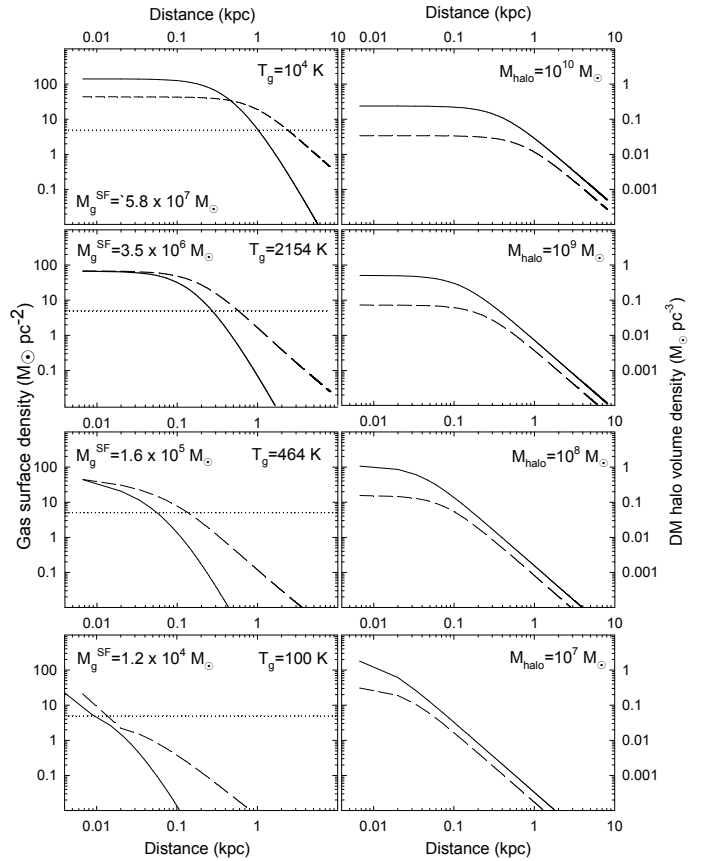


Fig. 8. Left column. Comparison of the gas surface density in the reference model (dashed lines) with that of the $z_{\text{gf}} = 2.0$ model (solid lines). The dotted line marks the critical surface density for star formation $\Sigma_c = 5 M_\odot \text{pc}^{-2}$. Gas temperature is indicated in every panel and the DM halo mass is shown in the corresponding panels on the right. The gas mass M_g^{SF} with number density greater than 1.0cm^{-3} is given only for the $z_{\text{gf}} = 2.0$ models. **Right column.** Volume density profiles of the quasi-isothermal DM halos of various mass (as indicated in each panel) at $z_{\text{gf}} = 0$ (dashed lines) and $z_{\text{gf}} = 2.0$ (solid lines).

smaller than the cosmological values. This means that varying the zero point of the $T_{\text{DM}} \propto M_{\text{DM}}^{2/3}$ relation, one can in principle achieve a good agreement with the Λ CDM theory.

To explore the second possibility, we assume that our model gas disk has a non-thermal support against gravity in the form of turbulence and magnetic pressure. For the sake of simplicity, we assume equipartition between the gas kinetic pressure P and the two sources of non-thermal support (but see Cox (2005)), which yields the effective gas pressure $P_{\text{eff}} = 3P = 3\rho_g \sigma_g^2$ (which would correspond to an effective velocity dispersion $\sigma_{\text{eff}} = \sqrt{P_{\text{eff}}/\rho_g} = \sqrt{3}\sigma_g$). The dash-dotted line in the bottom panel of Figure 9 presents the M_g^{\min} – M_{DM} relation for the case with the non-thermal support. It is evident that the corresponding gas masses increase considerably, in particular for models with $M_{\text{DM}} \leq 10^9 M_\odot$. The matter is that introducing the non-thermal support we effectively increase the gas pressure and the corresponding gas surface density profiles become shallower as compared to those without non-thermal support. This results in an overall increase in the gas mass of a steady-state gaseous configuration. Figure 9 also suggests that varying the magnitude of the non-thermal support one can achieve a good agreement with

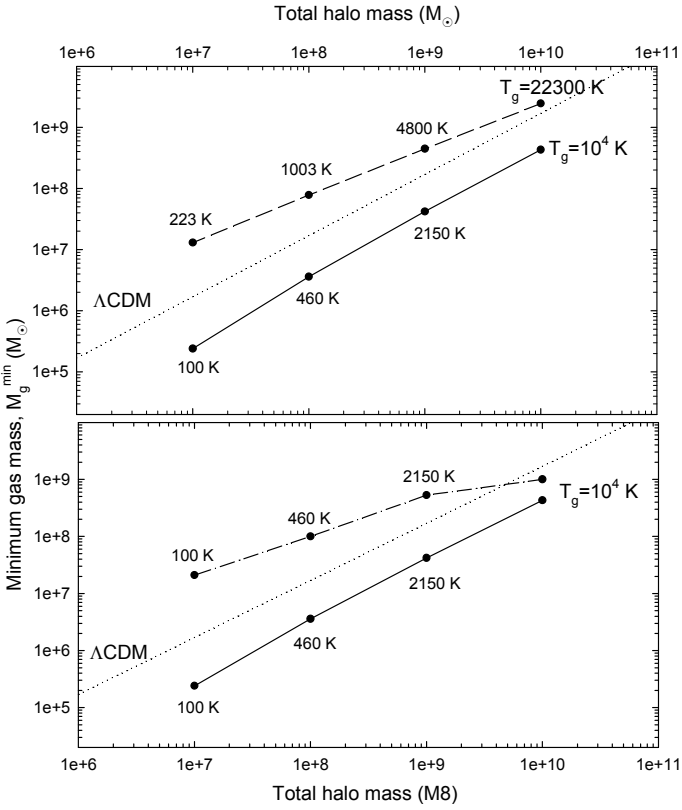


Fig. 9. Top. Effect of changing the zero-point of the $T_g \propto M_{\text{DM}}^{2/3}$ scaling law. The solid lines present the $M_{\text{g}}^{\text{min}}-M_{\text{DM}}$ relation for the reference model with scaling described by equation (19), whereas the dashed line does that for the scaling given by equation (24). The corresponding gas temperatures are indicated for each model. **Bottom.** The effect of non-thermal gas support against gravity. Solid lines show the $M_{\text{g}}^{\text{min}}-M_{\text{DM}}$ relation for the reference model (zero non-thermal support), whereas the dashed line does that for the models with the effective gas pressure three times greater than the gas kinetic pressure. The dotted line plots the cosmological relation between the baryonic and DM mass as suggested by the Λ CDM theory.

the cosmological mass of baryons given by the dotted line, particularly for galaxies with $M_{\text{DM}} \leq 10^{10} M_{\odot}$.

7. Implications for the evolution of dwarf galaxies

In this work, we have presented numerical solutions for equilibrium configurations of model galaxies made up of gas, stars and a DM halo in the combined gravitational potential of each of these components. The properties of these equilibrium configurations and, in particular, the minimum gas mass needed to achieve a state with allowed star formation $M_{\text{g}}^{\text{min}}$, have been considered in detail.

In future more detailed works, we will be using our derived equilibrium configurations as initial setups of galaxy models for which we will numerically study the detailed chemical and dynamical evolution, and also the effect of SF feedback. The interest in simulating the evolution of DGs is steadily growing in the last years. The reason is that Λ CDM theories of structure formation predict that dwarf galaxy-sized objects are the first virialized structures in the Universe. Moreover, the study of star formation and feedback in DGs is in many respects much simpler than in large spiral galaxies. Although studies

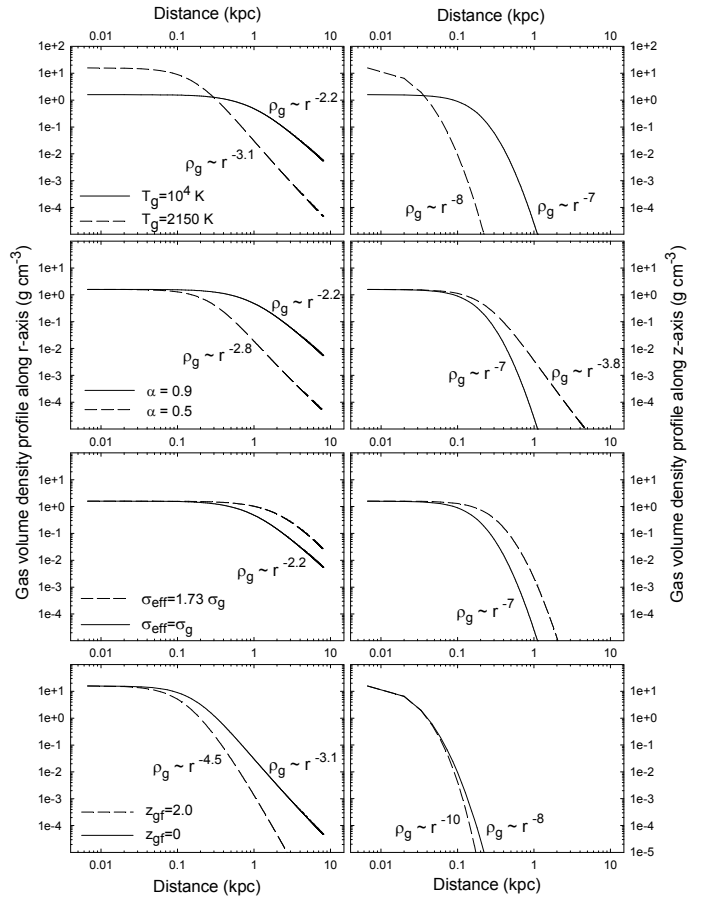


Fig. 10. Comparison of the gas volume density profiles along the r -axis (left column) and z -axis (right column). In particular, models in the top row are characterized by different gas temperatures T_g (as indicated), the second top row by different spin parameters α , the third top row by different effective gas dispersions σ_{eff} , and the bottom row by different redshift for galaxy formation z_{gf} . All other parameters for every model are the same (see text for more details).

of DGs in a cosmological context are more numerous and detailed than in the past (e.g. Kazantzidis et al., 2011; Sales et al., 2011; Pilkington et al., 2011; Governato et al., 2010), still they do not have enough spatial resolution to analyze in detail the internal evolutionary processes. A lot in resolution can be gained by zooming in and re-simulating small chunks of a large cosmological box (Martig et al., 2009; Sawala et al., 2011), but still the best way to accurately simulate a dwarf galaxy is by numerically studying it as a single isolated entity (Schroyen et al., 2011; Scannapieco & Brüggén, 2010; Revaz et al., 2009) although in reality they are subject to various environmental effects.

Although a quantitative comparison between our predictions and observations in DGs requires taking into account the feedback from star formation, yet our modeling can give us some insight as to the expected evolution of DGs. First, we note that for some models (especially the low-mass ones with $T=10^4$ K, see Figure 2, bottom row of panels) star formation is not expected to occur in the center of the galaxy, but only in a shell with inner radius between ≈ 100 pc and ≈ 1.0 kpc.

Second, the evolution of SN-driven shells is known to depend on the gas density distribution, which in turn is sensitive to the initial conditions in a dwarf galaxy. For instance, the Rayleigh-Taylor instability in the shell grows faster for steeper

gas density profiles. Figure 10 compares the gas *volume* density distributions ρ_g in star-formation-allowed models with different T_g , α , σ_{eff} , and z_{gf} . In particular, the left/right columns show the radial profiles of ρ_g taken along the r -/ z -axes. For the sake of conciseness, we consider only models with $M_{\text{DM}} = 10^9 M_{\odot}$, models with other DM halo masses show a similar behaviour. Models in the top row are characterized by $\alpha = 0.9$, $\sigma_{\text{eff}} = 0$, and $z_{\text{gf}} = 0$ (but different T_g as indicated in the Figure), models in the second top row by $T_g = 10^4$ K, $\sigma_{\text{eff}} = 0$, and $z_{\text{gf}} = 0$ (but different α), models in the third row by $T_g = 10^4$ K, $\alpha = 0.9$, and $z_{\text{gf}} = 0$ (but different σ_{eff}), and models in the bottom row by $T_g = 2150$ K, $\alpha = 0.9$, $\sigma_{\text{eff}} = 0$ (but different z_{gf}).

It is evident that taking a smaller gas temperature T_g or spin parameter results in equilibrium gas disks with a steeper tail of the gas volume density distribution. A similar effect is observed for models with a higher redshift for galaxy formation z_{gf} . On the other hand, models with and without non-thermal support have similar radial profiles of ρ_g . For every model considered, the vertical profiles of ρ_g are steeper than those taken along the horizontal axis, suggesting a blow-out effect along the rotational axis. The variety of possible model realizations implies that the evolution of DGs after the onset of star formation may follow different pathways depending on the initial conditions in the gas disk, even for the same DM halo mass.

8. Model caveats

8.1. Steady-state gaseous disks

A steady-state model is a first-order approximation to DGs galaxies. Various effect such as stellar feedbacks, non-axisymmetric density waves, and, in particular, external perturbations may drive DGs out of equilibrium. These phenomena can trigger star formation in otherwise quiescent gas disks and affect our derived values of M_g^{min} . In order to estimate the possible magnitude of such effects, we focus on perturbations with the conservation of the total gas mass¹⁰ and refer to star-formation-inactive models plotted in Figure 2 by black lines. It is evident that positive perturbations in Σ by a factor of 5–100 are needed to drive these models to the star formation threshold.

If perturbations of such amplitude are possible, then the critical gas mass required for star formation may be significantly lower. Indeed, as Figure 3 demonstrates, the total gas mass M_g of an equilibrium configuration declines with decreasing $n_{0,0}$. The filled squares mark the star-formation-allowed models, while the open circles correspond to the star-formation-inactive ones. If the $n_{0,0} = 0.01 \text{ cm}^{-3}$ models can be pushed to the star formation threshold, then the minimum mass for star formation M_g^{min} may be as low as $10^7 M_{\odot}$ for the $M_{\text{DM}} = 10^{10} M_{\odot}$ model. This corresponds to almost a factor of 40 decrease in the value of M_g^{min} as compared to the star-formation-allowed model with $n_{0,0} = 5 \text{ cm}^{-3}$. We note, however, this effect becomes considerably less pronounced for models with smaller DM halo masses. For instance, the corresponding decrease in M_g^{min} for the $M_{\text{DM}} = 10^7 M_{\odot}$ model is only a factor of 2.5. We conclude that high-amplitude density perturbations of the equilibrium state can significantly affect our estimates of M_g^{min} only for models with $M_{\text{DM}} \gtrsim 10^9 M_{\odot}$ but are of rather low significance for models with $M_{\text{DM}} \lesssim 10^8 M_{\odot}$.

¹⁰ Perturbations without conservation of the total mass, such as mergers or ram pressure stripping, can obviously affect our conclusions by changing the total available gas mass budget.

8.2. Multi-phase interstellar medium

In this study we have neglected the fact that the interstellar medium consists of various phases with usually different temperatures and considered a single-phase medium with some typical temperature T_g . Although cores of molecular clouds (where star formation occurs) have temperatures much lower than 10^4 K, the latter value must be seen as a mass-weighted mean temperature within each computational cell (which has a size much larger than the cores of molecular clouds). Indeed, the hot ($\sim 10^6$ K) and cold (\sim a few $\times 10$ K) gas phases usually amount to about 1% and 10% of the total gas mass reservoir, respectively (for the SF efficiency of $\sim 10\%$), meaning that the mean temperature is mostly determined by the warm gas phase. In this sense, $T_g = 10^4$ K represents a sort of an upper limit because it is impossible that a computational cell hosting (star-forming) regions with temperatures of few tens of K can have an average temperature significantly above 10^4 K. We note that lower than 10^4 K mean temperatures are, of course, possible, provided efficient cooling and low SF feedback.

One may argue that even though some models for $T_g = 10^4$ K may have difficulty to achieve critical densities for star formation, the differentiation into a multi-phase medium may eventually push a local region to star formation and that may trigger a chain reaction through the bulk of a galaxy. To account for this possibility, we have adopted an empirical star formation threshold by Kennicutt (2008). While the Toomre Q parameter criterion is based on the gravitational properties of a single-phase medium, the Kennicutt's criterion is based on observations of real multi-phase galaxies and hence takes implicitly into account the possibility of phase differentiation discussed above. In a comprehensive review, Hensler (2008) has discussed the advantages of a multi-phase treatment of the ISM in star-forming galaxy disks and emphasized the limitations of single gas-phase description.

8.3. Star formation criteria

In this paper, we have adopted three SF criteria, which are based on theoretical arguments, i.e., the Toomre gravitational stability criterion (16), and empirical evidence, i.e., the Kennicutt-Schmidt law (17). These SF criteria are not without limitations and observations suggest that SF can occur even in the Toomre-stable regions with $Q_{\text{T}} \gtrsim Q_{\text{c}}$, e.g., near the galactic center where the gravitational stability may be determined by the rate of shear rather than by the magnitude of epicycle motions (Vorobyov, 2003). Moreover, a few galaxies in the Kennicutt's (2008) sample harbour SF below the adopted gas density threshold of $\Sigma_{\text{c}} = 5 M_{\odot} \text{ pc}^{-2}$. At the lower end of the KS correlation the scatter of measurements also widens, because the SF rate fluctuates more stochastically and e.g. starbursting DGs are systematically located above the relation (see e.g. Hensler, 2012). In addition, it is well documented that the KS relation is tighter when the SF rate is correlated with the molecular hydrogen H_2 (Kennicutt et al., 2007; Bigiel et al., 2008).

Nevertheless, we can use the same arguments as in Section 8.1 to show that a factor of ten variation in the adopted value of Σ_{c} can significantly affect our estimates of M_g^{min} only in models with the DM halo mass $M_{\text{DM}} \gtrsim 10^9 M_{\odot}$ and the effect of uncertainty in Σ_{c} is diminishing for DM halos with smaller mass¹¹. The value of n_{c} is more uncertain and depends largely on numerical resolution. Our adopted value of 1.0 cm^{-3} com-

¹¹ Note that Q_{c} allows for a smaller variation of order unity.

plies with most numerical studies on galactic star formation and varying this value by a factor of 10 can produce only a factor of several variations in M_g^{\min} , owing to a rather weak dependence of the total gas mass on $n_{0,0}$ (see Fig. 3).

It is worth pointing out that the Kennicutt-Schmidt relation (17) is based on $H\alpha$ measurements, which only reveal the presence of massive stars in the SF regions. Recently, mostly thanks to the GALEX satellite, measurements of UV fluxes became available for dwarf galaxies. It turns out that below $\sim 10^{-2} M_\odot \text{ yr}^{-1}$, the SF rate determined by the $H\alpha$ measurements largely underestimates that based on UV fluxes (Lee et al., 2009). If the IMF in DGs is top-light (i.e. steeper than the Salpeter slope and with a small upper mass cutoff), $H\alpha$ fluxes can be very low even though SF is active (Pflamm-Altenburg et al., 2009). This can affect the threshold value for star formation Σ_c in equation (17).

9. Conclusions

We have constructed a series of rotating equilibrium galaxies consisting of gas, stars, and a fixed DM halo, with masses of the latter M_{DM} being in the $10^7 - 10^{10} M_\odot$ range. Our models differ from most previous studies in that we self-consistently take into account self-gravity of the gas component. Variations in the gas temperature, DM halo shape, rotation and non-thermal support, and also in the redshift for galaxy formation have been considered. We apply contemporary star formation criteria to the resulting equilibrium configurations to estimate the feasibility of large-scale star formation in our models. For the star formation criteria, we choose the Toomre gravitational stability criterion with the Toomre parameter smaller than a critical value of $Q_c = 2.0$ and the Kennicutt-Schmidt law with the gas surface density greater than a critical value of $\Sigma_{\text{crit}} = 5.0 M_\odot \text{ pc}^{-2}$. These criteria need to be satisfied simultaneously at least in some parts of the gas disk in order for the model to be marked as star-formation-allowed (SFA). In addition, we require that the gas mass with number density greater than $n = 1.0 \text{ cm}^{-3}$ exceed than $10^4 M_\odot$ to allow for a SF event of non-negligible magnitude.

We compare gas masses of the SFA models with the baryonic mass M_b derived from the Λ CDM theory and WMAP4 data, for which the ratio of the baryon-to-DM mass is 0.17. We find the following:

- For a given DM halo mass there exists a minimum gas mass M_g^{\min} that is needed to achieve a state in which star formation is allowed. The value of M_g^{\min} depends crucially on the gas temperature T_g , the gas spin parameter α , the amount of nonthermal support in the gas disk, and, to a somewhat lesser extent, on the redshift for galaxy formation z_{gf} . On the other hand, M_g^{\min} is rather insensitive to the form of the DM halo and to the pre-existing stellar disk, provided that the past SF efficiency does not exceed considerably 0.1.
- As a rule, M_g^{\min} is smaller for galaxies with smaller α and T_g and is greater for objects with greater non-thermal support σ_{eff} . In addition, M_g^{\min} may be smaller for objects that form at higher redshifts.
- Depending on the gas temperature T_g , gas spin parameter α , gas effective velocity dispersion σ_{eff} , and the redshift for galaxy formation z_{gf} , the SFA models may have M_g^{\min} that is either greater or smaller than M_b . Models with $M_{\text{DM}} \gtrsim 10^9 M_\odot$ are usually characterized by $M_g^{\min} \lesssim M_b$, implying that star formation in such galaxies is a natural outcome of their evolution. On the other hand, models with $M_{\text{DM}} \lesssim 10^9 M_\odot$ are often characterized by $M_g^{\min} \gg M_b$,

implying that they need much more gas than available according to the Λ CDM theory to achieve a state in which star formation is allowed.

- A good agreement of our derived M_g^{\min} with M_b can be achieved if the spatially uniform gas temperature follows the virial relation $T_g \propto M_{\text{DM}}^{2/3}$ with a proper choice of the zero point or some added non-thermal support. However, the required temperatures for objects with $M_{\text{DM}} \lesssim 10^8 M_\odot$ are quite low (\leq a few hundred Kelvin) and the rotation curves are in poor agreement with those observed in DGs.
- SFA models with $M_{\text{DM}} \lesssim 10^8 M_\odot$ and $T_g \gtrsim$ a few $\times 10^4$ K have M_g^{\min} that greatly exceed both M_b and M_{DM} , implying that some star-forming DGs may be baryon-dominated.

We find that the gas volume density distribution of our model galaxies is crucially sensitive to the gas temperature, spin parameter, and redshift of galaxy formation, implying a variety of possible equilibrium realizations for objects with the same DM halo mass. This means that the evolution of a dwarf galaxy may follow different pathways after the onset of star formation, depending on the values of T_g , α , and z_{gf} even for the same DM halo mass.

Our modeling suggests that a star-formation-allowed state is more difficult to achieve in DM halos with mass $\lesssim 10^9 M_\odot$ than in their upper-mass counterparts, because the required gas mass may be much greater than that available according to the Λ CDM theory. This implies that there may be a critical DM halo mass below which the likelihood of star formation and hence the total stellar mass drops substantially. Interestingly enough, the stellar versus DM halo mass relation recently derived by Guo et al. (2010) using the SDSS survey and Millennium Simulations implies the existence of such a threshold value. On the other hand, DGs with the gas plus stellar mass greater than that of the DM halo are not unheard of and recent observations of the mass-to-light ratios in Virgo Cluster dwarf ellipticals by Toloba et al. (2011) and in gas-rich DGs by Swaters et al. (2011) point to the existence of such objects. These observations, along with our results, suggest that the Λ CDM paradigm is not universal and significant deviations from the corresponding M_b - M_{DM} trend are feasible.

Our study outlines the importance of gas self-gravity (neglected in practically all hydrodynamical studies of isolated DGs) in building equilibrium galaxies. The main argument in favour of neglecting the gas self-gravity has been based on the assumption that the total gas mass is always much smaller than that of the DM halo. As we have demonstrated, this assumption may be grossly violated, particularly for low-mass DM halos with $M_{\text{DM}} \leq 10^8 M_\odot$. The reason is that the baryonic matter has to dominate the dark matter in objects with low DM halo masses in order to achieve the Kennicutt-Schmidt SF criterion. We emphasize that our results are strictly applicable to DM halos that have accumulated their mass reservoir quasi-statically and remain to be justified for object that have undergone a series of violent mergers. At the same time, our main conclusions are not affected by moderate perturbations in a quasi-equilibrium state and reasonable variations in the adopted values of Σ_{crit} and Q_c .

10. Acknowledgments

The authors are thankful to the referee for an insightful report that helped to considerably improve the manuscript. This publication is supported by the Austrian Science Fund (FWF). EV thanks a Lise Meitner Fellowship (Austrian Science Fund

FWF), project number M 1255-N16 for financial support. Numerical simulations were done on the Atlantic Computational Excellence Network (ACEnet) and on the Shared Hierarchical Academic Research Computing Network (SHARCNET).

References

- Banerjee, A., Jog, C. J., Brinks, E., & Bagetakos, I. 2011, *MNRAS*, 415, 687
 Barnabé M., Ciotti, L., Fraternali, F., Sancisi, R. 2009, *A&A*, 446, 61
 Bigiel, F., Leroy, A., Walter, F., et al. 2008, *Astron. J.*, 136, 2846
 Black, D. C., Bodenheimer, P. 1975, *ApJ*, 199, 619
 Bodenheimer, P., & Ostriker, J. P. 1973, *ApJ*, 180, 159
 Brinks, E., & Burton, W. B. 1984, *A&A*, 141, 195
 Burkert, A. 1995, *ApJ*, 447, L25
 Carignan, C., & Beaulieu, S. 1989, *ApJ*, 347, 760
 Cattaneo, A., Mamon, G.A., Warnick, K., & Knebe, A. 2011, *A&A*, 533, A5
 Chandrasekhar, S. 1969, *Ellipsoidal figures of equilibrium*, Yale University Press
 Cox, D. P. 2005, *ARA&A*, 43, 377
 de Blok, W. J. G., McGaugh, S. S., Bosma, A., & Rubin, V. C. 2001, *ApJ*, 552, L23
 de Blok, W. J. G., Walter, F., Brinks, E., et al. 2008, *AJ*, 136, 2648
 D’Ercole, A., & Brighenti, F. 1999, *MNRAS*, 309, 941
 Dong, H., Calzetti, D., Regan, M., et al. 2008, *Astron. J.*, 136, 497
 Elmegreen, B. 1997, in *Starburst Activity in Galaxies*, ed. J. Franco, R. Terlevich, & A. Serrano, *Rev. Mex. Astron. Astrophys. Conf. Ser.*, 6, 165
 Fujita, A., Martin, C. L., Mac Low, M.-M., & Abel, T. 2003, *ApJ*, 599, 50
 Governato, F., Brook, C., Mayer, L., et al. 2010, *Nature*, 463, 203
 Guo, Q., White, S., Li, C., Boylan-Kolchin, M. 2010, *MNRAS*, 404, 1111
 Harfst, S., Theis, C., & Hensler, G. 2006, *A&A*, 449, 509
 Hensler, G., 2008, *Proceed. IAU Symp. No. 254*, J. Andersen, J. Bland-Hawthorn, & B. Nordstrom (Eds.), Cambridge Univ. Press, p. 269
 Hensler, G. 2012, *Proceed. Symp. 3 Dwarf Galaxies: Keys to Galaxy Formation and Evolution*, at JENAM 2010 in Lisbon, P. Papaderos, S. Recchi, & G. Hensler (eds.), Springer Publ., in press
 Kalberla, P.M.W., & Kerp, J. 2009, *ARA&A*, 47, 27
 Kazantzidis, S., Lokas, E. L., Mayer, L., Knebe, A., & Klimentowski, J. 2011, *ApJ*, 740, L24
 Kennicutt, R. C. 1998, *ApJ*, 498, 541
 Kennicutt, R.C., Calzetti, D., & Walter, F. 2007, *ApJ*, 671, 333
 Kennicutt, R. C. 2008, in *Pathways Through an Eclectic Universe*, ASP Conference Series, Vol. 390, pg. 149
 Kent, S. M., Dame, T. M., & Fazio, G. 1991, *ApJ*, 378, 131
 Kim W.-T., E. Ostriker 2001, *ApJ*, 559, 70
 Kroupa, P., Famaey, B., de Boer, K. S., et al. 2010, *A&A*, 523, A32
 Lebovitz, N. R. 1967, *ARA&A*, 5, 465
 Lee, J. C., Gil de Paz, A., Tremonti, C., et al. 2009, *ApJ*, 706, 599
 Leroy, A.K., Walter, F., Brinks, E., et al. 2008, *Astron. J.*, 136, 2782
 Lindblom, L. 1992, *Royal Society of London Philosophical Transactions Series A*, 340, 353
 Mac Low, M.-M., Ferrara, A. 1999, *ApJ*, 513, 142
 Marcolini, A., Brighenti, F., & D’Ercole, A. 2003, *MNRAS*, 345, 1329
 Martig, M., Bournaud, F., Teyssier, R., & Dekel, A. 2009, *ApJ*, 707, 250
 Narayan, C. A., & Jog, C. J. 2002, *A&A*, 394, 89
 Navarro, J. F., Frenk, C. S., & White S. D. M. 1997, *ApJ*, 490, 493
 Navarro, J. F., Ludlow, A., Springel, V., et al. 2010, *MNRAS*, 402, 21
 Neto, A. F. et al. 2007, *MNRAS*, 381, 1450
 O’Brien, J. C., Freeman, K. C., & van der Kruit, P. C. 2010, *A&A*, 515, A62
 Oh, S.-H., de Blok, W.J.G., Walter, F., Brinks, E., & Kennicutt, R.C. 2008, *AJ*, 136, 2761
 Papaderos, P., Guseva, N.G., Izotov, Y.I., & Fricke, K.J. 2008, *A&A*, 491, 113
 Papaderos, P., Loose, H.-H., Fricke, K. J., & Thuan, T. X. 1996, *A&A*, 314, 59
 Pflamm-Altenburg, J., Weidner, C., & Kroupa, P. 2009, *MNRAS*, 395, 394
 Pilkington, K., Gibson, B. K., Calura, F., et al. 2011, *MNRAS*, 417, 2891
 Polyachenko V. L., Polyachenko E. V., Strelnikov A. V., 1997, *Astron. Zhurnal*, 23, 551 (translated *Astron. Lett.* 23, 483)
 Recchi, S., Matteucci, F., & D’Ercole, A. 2001, *MNRAS*, 322, 800
 Revaz, Y., Jablonka, P., Sawala, T., et al. 2009, *A&A*, 501, 189
 Roychowdhury, S., Chennugulati, J.N., Begum, A., & Karachentsev, I.D. 2009, *MNRAS*, 397, 1435
 Salucci, P., & Burkert, A. 2000, *ApJ*, 537, L9
 Sancisi, R., & Allen, R. J. 1979, *A&A*, 74, 73
 Sales, L. V., Navarro, J. F., Cooper, A. P., et al. 2011, *MNRAS*, 418, 648
 Sawala, T., Guo, Q., Scannapieco, C., Jenkins, A., & White, S. 2011, *MNRAS*, 413, 659
 Scannapieco, E., & Brügggen, M. 2010, *MNRAS*, 405, 1634
 Shaye, J. Dalla Vecchia, C. 2008, *MNRAS*, 383, 1210

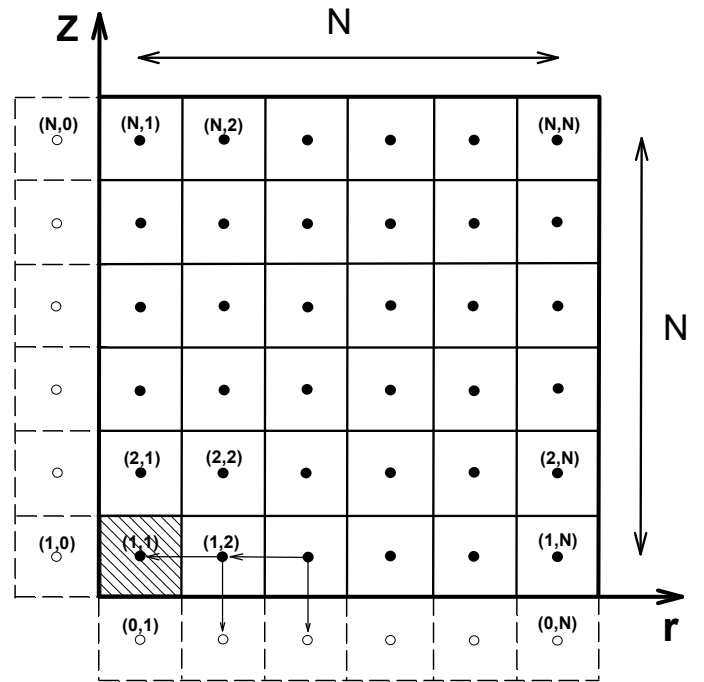


Fig. A.1. Computational domain in the (r, z) plane showing active and ghost grid zones with solid and dashed lines, respectively. The zone centers are marked with filled/open circles for active/ghost zones. The arrows indicate the backward finite-difference scheme used to discretize spatial derivatives. The innermost grid cell highlighted with a backslash palette refers to the seed value of the gas surface density $n_{0,0}$.

- Schroyen, J., de Rijcke, S., Valcke, S., Cloet-Osselaer, A., & Dejonghe, H. 2011, *MNRAS*, 416, 601
 Silich, S., Tenoreo-Tagle, G. 2001, *ApJ*, 552, 91
 Spekkens, K., Giovanelli, R., & Haynes, M. P. 2005, *AJ*, 129, 2119
 Spergel, D.N., Verde, L.L., Peiris, H.V., et al. 2003, *ApJS*, 148, 175
 Springel, V., Hernquist, L. 2003, *MNRAS*, 339, 289
 Stone, J. M., Norman, M. L. 1992, *ApJSS*, 80, 753
 Strickland, D. K., & Stevens, I. R. 2000, *MNRAS*, 314, 511
 Suchkov, A. A., Balsara, D. S., Heckman, T. M., & Leitherer, C. 1994, *ApJ*, 430, 511
 Swaters, R. A., Sancisi, R., van Albada, T. S., & van der Hulst, J. M. 2009, *A&A*, 493, 872
 Swaters, R. A., Sancisi, R., van Albada, T. S., & van der Hulst, J. M. 2011, *ApJ*, 729, 118
 Takeuchi, T.T., Hirashita, H., Ishii, T.T., Hunt, L.K., & Ferrara, A. 2003, *A&A*, 343, 839
 Tasker, E. J. 2011, *ApJ*, 730, 11
 Tassoul, J.L. 1978, *Theory of rotating stars*, Princeton University Press
 Thomas, D., Maraston, C., Bender, R., & Mendes de Oliveira, C. 2005, *ApJ*, 621, 673
 Toloba, E., Boselli, A., Cenarro, A.J., et al. 2011, *A&A*, 526, A114
 Tomisaka, K. & Ikeuchi, S. 1988 *ApJ*, 330, 695
 Toomre A., 1964, *ApJ*, 139, 1217
 Vasiliev, E. O., Vorobyov, E. I., & Shchekinov Yu. A. 2008, *A&A*, 489, 505
 Vorobyov, E. I. 2003, *A&A*, 407, 913
 Vorobyov E. I., Klein U., Shchekinov Yu. A., Ott J., 2004, *A&A*, 413, 939
 Vorobyov, E. I., Basu, S. 2005, *A&A*, 431, 451
 van Zee, L., Westpfahl, D., Haynes, M.P., & Salzer, J.J. 1998, *AJ*, 115, 1000

Appendix A: Solving for the steady-state equations

Figure A.1 shows the $N \times N$ computational mesh employed to discretize the steady-state equations (3) and (4). The active zones are outlined with the solid lines, whereas the two rows of ghost zones (representing the reflecting boundary conditions along the

z - and r -axes) are marked with the dashed lines. The active/ghost zone centers are denoted with filled/open circles.

A class of problems that does not require the knowledge of the gas density at the outer z and r boundaries (i.e., at $N + 1$ grid zones) can be solved using the following procedure. We use a first-order backward difference scheme (schematically shown by the arrows) to obtain a finite-difference representation of equations (3) and (4) for the case with a spatially uniform σ_g

$$\begin{aligned} \frac{\ln \rho_g^{(i,j)} - \ln \rho_g^{(i,j-1)}}{\Delta r_j} &= \frac{1}{\sigma_g^2} \left[\frac{v_g^{2,(i,j-1/2)}}{r_{j-1/2}} + g_{g,r}^{(i,j-1/2)} + g_{h,r}^{(i,j-1/2)} \right] \\ \frac{\ln \rho_g^{(i,j)} - \ln \rho_g^{(i-1,j)}}{\Delta z_i} &= \frac{1}{\sigma_g^2} \left[g_{g,z}^{(i-1/2,j)} + g_{h,z}^{(i-1/2,j)} \right], \end{aligned} \quad (\text{A.1})$$

where the indices i and j correspond to the z and r coordinate directions, respectively. We note that densities are defined at the zone centers while gravitational accelerations and velocities are defined at the corresponding zone interfaces. In order for this difference scheme to work, one needs to define the gas density at the ghost zones (which equal to those at the nearest active zones) and also the gas density at the innermost active zone (1, 1) denoted in the paper as the seed density $n_{0,0}$. The corresponding zone is highlighted with the backslash palette in Figure A.1.

With this choice of the discretization scheme and boundary conditions, one can notice that $\rho_g^{(i,j-1)}$ and $\rho_g^{(i-1,j)}$ are known for every value of $\rho_g^{(i,j)}$ and the latter can be found by a fast forward substitution algorithm if one proceeds from left to right along the r -direction, starting from the bottom layer of zones and advancing one horizontal layer after another in the direction of increasing z .

Appendix B: Testing equilibrium configurations

An important reliability check on the solution procedure is to test how our equilibrium configurations can be handled by time-dependent numerical hydrodynamics codes. If our steady-state models are correct, than a galaxy should stay in rotational equilibrium for at least 500 Myr, a typical time of interest when simulating the effect of supernova explosions in DGs.

To perform such a test, we use our time-dependent numerical hydrodynamics code employed earlier to study the effect of SN explosions in DGs in the local Universe and and large redshifts (Vorobyov et al., 2004; Vorobyov & Basu, 2005; Vasiliev et al., 2008). We intentionally turn off cooling and heating to avoid the system drifting out of equilibrium due to thermal effects. For the test, we use the reference model with $M_{\text{DM}} = 10^9 M_\odot$, $\alpha = 0.9$, $T_g = 10^4$ K, and $n_{0,0} = 5.0 \text{ cm}^{-3}$. The gas surface density, Q parameter, and velocity profiles of this model are shown by the red solid lines in the second top row of Figure 2.

Figure B.1 shows the mean relative error (solid line) and the maximum relative error (dashed line) in the gas volume density ρ_g (top) as a function of time t in our test model. The relative errors (in per cent) are calculated at every grid cell as¹²

$$\Delta \rho_{g,i,j} = \frac{|\rho_{g,i,j}(t) - \rho_{g,i,j}(0)|}{\rho_{g,i,j}(0)} \quad (\text{B.1})$$

and demonstrate the degree to which our equilibrium is held by the code during the time evolution. The mean relative errors $\Delta \rho_g$

¹² An extended definition of the relative error that takes into account a situation when the gas density declines with time, and is thus normalized to the current value of $\rho_g(t)$ rather than to the initial one $\rho_g(0)$, yields very similar results.

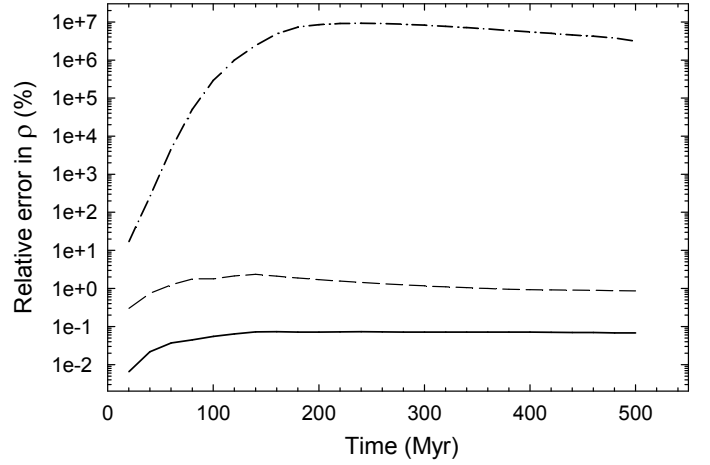


Fig. B.1. Maximum and mean relative errors (dashed and solid lines, respectively) in the gas volume density (top) as functions of time t for the reference test model described in Appendix B. The errors are calculated relative to the initial equilibrium configuration at $t = 0$ Myr. The dash-dotted lines show the relative errors in the absence of gas self-gravity.

are calculated by averaging the individual errors $\Delta \rho_{g,i,j}$ over the entire computational grid. As one can see, the mean relative errors never exceed 0.1%, meaning the equilibrium is well preserved globally. The maximum relative error never exceeds 3% and is kept below 1% during most of the evolution. We note the maximum errors occur in dynamically unimportant regions near the axes at large ϖ . The gas temperature shows essentially the same behaviour. This test convincingly proves the robustness and reliability of our solution procedure.

To demonstrate the importance of gas self-gravity and to perform the final check on our self-gravitating equilibrium configurations, we artificially turn off the gas self-gravity in our time-dependent numerical hydrodynamics code. The dash-dotted lines in Figure B.1 present the resulted mean relative error. It is obvious that neglecting the gas self-gravity results in a complete destruction of the equilibrium state, with the mean relative errors exceeding 10^6 for the gas volume density!